Thermal properties of large main-belt asteroids observed by Herschel PACS

V. Alí-Lagoa[1], T. G. Müller[1], C. Kiss[2, 3], R. Szakáts[2], G. Marton[2, 3], A. Farkas-Takács[2, 4], P. Bartczak[5], M. Butkiewicz-Bąk[5], G. Dudziński[5], A. Marciniak[5], E. Podlewska-Gaca[5], R. Duffard[6], P. Santos-Sanz[6], and J. L. Ortiz[6]

[1] Max-Planck-Institut für extraterrestrische Physik, Giessenbachstrasse 1, 85748 Garching, Germany
e-mail: `vali@mpe.mpg.de`
[2] Konkoly Observatory, Research Centre for Astronomy and Earth Sciences, Konkoly Thege Miklós út 15-17, H-1121 Budapest, Hungary
[3] ELTE Eötvös Loránd University, Institute of Physics, Pázmány Péter sétány 1/A, H-1117 Budapest, Hungary
[4] Eötvös Loránd University, Faculty of Science, Pázmány Péter sétány 1/A, H-1117 Budapest, Hungary
[5] Astronomical Observatory Institute, Faculty of Physics, A. Mickiewicz University, Słoneczna 36, 60-286 Poznań, Poland.
[6] Instituto de Astrofísica de Andalucía (CSIC), Glorieta de la Astronomía s/n, 18008 Granada, Spain

ABSTRACT

Non-resolved thermal infrared observations enable studies of thermal and physical properties of asteroid surfaces provided the shape and rotational properties of the target are well determined via thermo-physical models. We used calibration-programme Herschel PACS data (70, 100, 160 μm) and state-of-the-art shape models derived from adaptive-optics observations and/or optical light curves to constrain for the first time the thermal inertia of twelve large main-belt asteroids. We also modelled previously well-characterised targets such as (1) Ceres or (4) Vesta as they constitute important benchmarks. Using the scale as a free parameter, most targets required a re-scaling ~5% consistent with what would be expected given the absolute calibration error bars. This constitutes a good cross-validation of the scaled shape models, although some targets required larger re-scaling to reproduce the IR data. We obtained low thermal inertias typical of large main belt asteroids studied before, which continues to give support to the notion that these surfaces are covered by fine-grained insulating regolith. Although the wavelengths at which PACS observed are longwards of the emission peak for main-belt asteroids, they proved to be extremely valuable to constrain size and thermal inertia and not too sensitive to surface roughness. Finally, we also propose a graphical approach to help examine how different values of the exponent used for scaling the thermal inertia as a function of heliocentric distance (i.e. temperature) affect our interpretation of the results.

Key words. minor planets, asteroids: general – surveys – infrared: planetary systems

1. Introduction

Non-resolved observations of asteroid thermal infrared (IR) emission provide information about the asteroid sizes and the thermal properties of their surfaces. By taking into account asteroid shape, rotation, and the geometry of the observations, thermo-physical models (TPMs) can be used to compute surface temperatures and fit thermal properties, such as thermal inertia, to the IR data. The number of asteroids with a thermo-physical characterisation has increased greatly over the last two decades thanks to the ever growing number of available shape and rotational models – which are necessary input for the TPM – and great observational efforts, both in the visible and the thermal IR (for recent reviews see e.g. Delbo et al. 2015; Ďurech et al. 2015; Mainzer et al. 2015, and references therein).

The number of available shape models, by which we refer to both shape and rotational properties, is dominated by the several hundred models derived from the inversion of non-resolved optical light curves (e.g. Ďurech et al. 2010; Ďurech et al. 2018; Hanuš et al. 2011, 2013) following the method by Kaasalainen & Torppa (2001) (see also Kaasalainen et al. 2001, 2002). Increasingly more sophisticated algorithms have begun to combine various data types in the inversion (Carry et al. 2010; Ďurech et al. 2011; Viikinkoski et al.

2015; Bartczak & Dudziński 2018), even thermal IR data (Ďurech et al. 2017; Müller et al. 2017), and there are now dozens of models based also on stellar occultations, radar, and adaptive optics observations (e.g. Ďurech et al. 2015; Benner et al. 2015, and references therein).

As the availability of asteroid shape models continues to increase, we can readily make use of a large collection of thermal IR data from several catalogues like those provided by the Infrared Astronomical Satellite (IRAS), AKARI, or the Wide-field Infrared Survey Explorer (WISE). Up to 2018, targeted observations from ground- and space-based facilities (e.g. Müller 2002; Müller & Blommaert 2004; Emery et al. 2006; Müller et al. 2017; Landsman et al. 2018) and/or from all-sky thermal IR surveys (e.g. Delbo' & Tanga 2009; Alí-Lagoa et al. 2014; Rozitis et al. 2014; Hanuš et al. 2015, 2016; Bach et al. 2017; Marciniak et al. 2018) had been used to model ~100 asteroids with TPMs. With the recent addition of another 100 (Hanuš et al. 2018b), WISE data are now the single largest source of asteroid thermal inertias.

Our aim in this work is to provide a thermo-physical characterisation of main-belt asteroids (MBAs) with Herschel Photodetector Array Camera and Spectrometer (PACS) data taken during the Asteroid Preparatory Programme for Herschel, ASTRO-F and the Atacama Large Millimiter/submilimiter ar-

ray (Müller et al. 2005a). Only a fraction of this data set has been exploited so far, for example in the context of absolute infrared flux calibration using well-characterised asteroids (Müller et al. 2014), or in studies of specific targets (e.g. O'Rourke et al. 2012; Marsset et al. 2017). The PACS data are important not only in terms of quality and additional wavelength coverage, but because their combination with AKARI and IRAS data allows us to bring the number of large MBAs analysed via a TPM closer to completeness[1].

This work was possible thanks to (i) the availability of a set of new shape models derived using the All-Data Asteroid Modelling (ADAM) (Viikinkoski et al. 2015) and the Shaping Asteroids with Genetic Evolution (SAGE) (Bartczak et al. 2014; Bartczak & Dudziński 2018) algorithms and (ii) the expert-reduced data products submitted to the Herschel Science Archive, which include some targets for which a non-standard data reduction approach was required[2]. Such data reduction and the creation of a large database featuring IRAS, AKARI, and WISE data (Szakáts et al. 2020) have been carried out in the framework of the "Small Bodies: Near and Far" (SBNAF) project (Müller et al. 2018), funded by the European Commission. SBNAF aimed at exploiting synergies between different small-body modelling techniques that use a wide range of data types from ground and space observatories (stellar occultations, visible and thermal infrared photometry, etc.) to produce physical models of the selected targets, which range from near-Earth asteroids to trans-Neptunian objects.

In Sect. 2 we briefly describe the IR data set and in Sect. 3 the TPM approach and simplifying assumptions. In Sect. 4 we present our results and in Sect. 5 we provide further discussion and comments. Appendix A contains plots relevant to the TPM analysis and Appendix B a table with all the Herschel PACS data used in this work.

2. Data

In this section we give a brief summary of the IR data. Further details of the Herschel PACS (Pilbratt et al. 2010; Poglitsch et al. 2010) catalogue of asteroid observations (Müller et al. 2005b) can be found in Müller et al. (2014), who already published the PACS data of (1) Ceres, (2) Pallas, (4) Vesta, and (21) Lutetia, which were used as IR calibrators in that work. In addition, information about the more specialised data reduction approach required for some PACS measurements is already available from the User Provided Data Products release note of the main-belt asteroid expert-reduced data products submitted to the Herschel Science Archive by Kiss, Müller and Farkas-Takács[2].

We also used whatever data was available from the IRAS and Midcourse Space Experiment (MSX) (Tedesco et al. 2002b,a), AKARI Infrared Camera (Murakami et al. 2007; Takita et al. 2012; Usui et al. 2011; Hasegawa et al. 2013), and WISE catalogues (W3 and W4 data; Mainzer et al. 2011; Masiero et al. 2011; Wright et al. 2010) [3]. We used all colour-corrected flux densities and absolute calibration error bars compiled in the SB-NAF thermal infrared database (IRDB). Szakáts et al. (2020)

provide all relevant details about the production of the IRDB[4], including the colour correction approach, sources and references of each catalogue, and useful auxiliary quantities such as observation geometry, and light-travel time. For completeness, Table B.1 provides all previously unpublished PACS observations used in this work.

3. Thermo-physical model implementation

Our TPM implementation is the one used by (Alí-Lagoa et al. 2015) based on that of Delbo' et al. (2007) and Delbo' & Tanga (2009). Said version was upgraded to account for the effects of shadowing, but global self-heating was neglected for this work (see e.g. the discussion about average view factors by Rozitis & Green 2013). Below we provide only a brief summary of the technique that we use and the approximations that we make. Our methodology was described in more length in Marciniak et al. (2018) and Marciniak et al. (2019). There, details about the thermo-physical modelling of each target were provided in separate sections. Here, we only present some relevant plots in the main text and include all TPM-related plots and additional comments in Appendix A.

We take a shape model as input for our TPM (see Table 1) with the main goal of modelling the surface temperature distribution at epochs at which we have thermal IR observations and constrain the target's diameter, thermal inertia and, whenever possible, surface roughness. From the known geometry of observation we identify which surface elements (usually triangular facets) were visible to the observer at each epoch and compute the model fluxes from the surface temperature distribution.

To account for heat conduction towards the subsurface, we solve the 1D heat diffusion equation for each facet and we use the Lagerros approximation when modelling the surface roughness via hemispherical craters of different depth covering 0.6 of the area of each facet (Lagerros 1996, Lagerros 1998, Müller & Lagerros 1998, Müller 2002). We also consider the spectral emissivity to be 0.9 regardless of the wavelength (see e.g. Delbo et al. 2015).

For each target, we estimated the Bond albedo (necessary input) as the average value obtained from the different radiometric diameters available from AKARI and/or WISE (Usui et al. 2011; Alí-Lagoa et al. 2018; Mainzer et al. 2016), and all available H-G, H-G_{12}, and H-G_1-G_2 values from the Minor Planet Center, Oszkiewicz et al. (2011), or Vereš et al. (2015).

This approach leaves us with two free parameters, the scale of the shape (interchangeably called the diameter, D) and the thermal inertia (Γ). The diameters and other relevant information related to the TPM analyses of our targets are provided in Table 2. Whenever the data are too few to provide realistic error bar estimates, we report the best fitting diameter so that the models can be scaled and compared to the scaling given by the occultations. On the other hand, if we have multiple good-quality thermal data (with absolute calibration errors below 10%) then this typically translates to a size accuracy of around 5% as long as the shape is not too extreme and the spin vector is reasonably well established. This rule of thumb certainly works for large MBAs like the Gaia mass targets. We do not consider the errors introduced by the pole orientation uncertainties or the shapes (see Hanuš et al. 2015 and Bartczak & Dudziński 2019), so our TPM error bars estimates are lower values.

---

[1] Large MBAs were too bright for WISE and their partially saturated fluxes might not be optimal for thermo-physical modelling. On the other hand, partial saturation can be corrected for and reasonably suited for thermal modelling purposes (e.g. Masiero et al. 2011; Mainzer et al. 2015).

[2] `http://archives.esac.esa.int/hsa/legacy/UPDP/SBNAF_MBA/SBNAF_MBA_Release_Note.pdf`

[3] For (21) Lutetia (see Sect. A.4), we also included most of the data analysed in O'Rourke et al. (2012).

[4] https://ird.konkoly.hu/

Table 1. Origin and references for the shape models.

Asteroid	Model	Reference
(1) Ceres	Dawn	Park et al. (2019)[a]
(2) Pallas	ADAM	Hanuš et al. (2017)[b]
(3) Juno	ADAM	Viikinkoski et al. (2015)[b]
(3) Juno	SAGE	Podlewska-Gaca et al. (2020)[c]
(4) Vesta	Dawn	Gaskell[d]
(8) Flora	ADAM	Hanuš et al. (2017)[b]
(10) Hygiea	ADAM	Vernazza et al. (2019)
(18) Melpomene	ADAM	Hanuš et al. (2017)[b]
(19) Fortuna	ADAM	Hanuš et al. (2017)[b]
(20) Massalia	SAGE 1, 2	Podlewska-Gaca et al. (2020)[c]
(21) Lutetia	Rosetta	Jorda (Farnham 2013)
(29) Amphitrite	ADAM	Hanuš et al. (2017)[b]
(52) Europa	ADAM	Hanuš et al. (2017)[b]
(54) Alexandra	ADAM	Hanuš et al. (2017)[b]
(65) Cybele	ADAM	Viikinkoski et al. (2017)[b]
(88) Thisbe	ADAM	Hanuš et al. (2017)[b]
(93) Minerva	ADAM	Hanuš et al. (2017)[b]
(423) Diotima	ADAM	Hanuš et al. (2018a)[b]
(511) Davida	ADAM	Viikinkoski et al. (2017)[b]

Notes. [a] Downloaded from the PDS. `https://pds.nasa.gov/`
[b] Downloaded from the DAMIT database
`https://astro.troja.mff.cuni.cz/projects/damit/`
(Ďurech et al. 2010) [c] Available from the ISAM service
`http://isam.astro.amu.edu.pl` (see Marciniak et al. 2012,
for details). [d] Downloaded from the Dawn Public Data site
`http://dawndata.igpp.ucla.edu/tw.jsp?section=geometry/ShapeModels`

4. Results

Table 2 summarises the thermophysical properties obtained for
each target in our sample. For comparison, we also include the
results for the spheres with the same rotational properties as the
shape models. All plots produced during the modelling and fur-
ther details about some selected targets are provided in Appendix
A. In this section we provide a summary of the results and focus
on several aspects relevant to the sample and/or a larger cata-
logue of thermo-physical properties retrieved from the literature.
For example, the thermal inertia versus size plot (Fig. 1) shows
that our new thermal inertias fall within the same range of those
of other large MBAs found in previous works.

Most ADAM shape models only required a small re-scaling
of the size to fit the data with low $\bar{\chi}^2_{\min}$, which we take as an
additional confirmation of their high quality. However, in the
cases of (65) Cybele, (18) Melpomene, and (54) Alexandra, we
required re-scalings of the order of 10% to fit the data, which
are larger than expected for the available high-quality thermal
data and shape models (e.g. Delbo et al. 2015). Thus, regard-
less of their quality, it is still worthwhile keeping the scale as
a free parameter when performing thermo-physical modelling
using already-scaled shape models in order to check potential is-
sues. For example, the ADAM shape of Pallas with a fixed scale
could not reproduce well PACS data taken closer to pole-on, as
illustrated in Figs. 2 and 3. The first one shows the observation-
to-model ratios (OMR) versus aspect angle for our best fit, that
is $\Gamma = 30\,\mathrm{J\,m^{-2}\,s^{-1/2}K^{-1}}$ and a re-scaling of +3%. The second
one shows the best fit obtained with a fixed scale, which led to
$\Gamma = 8\,\mathrm{J\,m^{-2}\,s^{-1/2}K^{-1}}$. Although this fit is also formally accept-
able, the OMRs are only close to one at equatorial views (aspect
angles around 90 degrees). No other combination of thermal in-
ertia and roughness could bring the other ratios closer to unity,
which suggests that the shape model could be less accurate at

pole-on views. In this particular case, this could also explain the
lower thermal inertia needed to fit the data when we kept the
scale fixed, because the data taken at higher phase angles were
coincidentally the ones taken at non-equatorial sub-observer lat-
itudes, which makes it more difficult for the shape model to re-
produce the thermal phase curve (see Fig. 4).

We found formally good fits and thermal properties within
the expected range for the two targets with SAGE models avail-
able for our study as well, albeit with slightly higher error bars.
Additional SAGE models scaled using stellar occultation chords
and further discussion are provided by Podlewska-Gaca et al.
(2020). It is worth mentioning that the TPM did not help us to
favour any of the two mirror shape solutions of (20) Massalia.

For each shape model, we also fitted the data using spheres
with the corresponding rotational parameters with the aim of
comparing the resulting thermo-physical parameters (see Table
2). On the one hand, this approximation seems to provide rea-
sonable estimates for the diameters that would be expected for
large objects with relatively low-amplitude light curves. On the
other hand, spheres lead to scales ~5% larger on average than the
ADAM shapes, and several of the thermal inertia values were up
to an order of magnitude higher than those of the correspond-
ing shape models. With the current sample we could not identify
any single cause that should lead to such systematic effects, but
perhaps a future larger sample could help explore this further.
Also, this could be used to create a reliable benchmark to esti-
mate thermal inertias of objects with more limited shape models.

4.1. Thermal inertia, pole-on views, and rotational variability

Only those asteroids with highly oblique rotational axes (or al-
ternatively, unusually high orbital inclinations) can be seen with
aspect angles close to pole-on, that is, 0 or 180 degrees for the
north and the south pole. In these cases, seasonal effects on the
surface temperature distribution are expected, since the depth at
which the heat wave penetrates is higher at close to pole-on illu-
minations. In principle, data taken in such circumstances could
require a model accounting for thermal inertia variation with
depth (such as those used for the Moon; Hayne et al. 2017), but
our OMR versus aspect angle plots do not suggest problems in
fitting data taken at close to pole-on views (e.g. see Fig. 2). We
did not find any correlation between Γ and the pole ecliptic lat-
itude either. The vast majority of OMR versus rotational phase
plots suggest that the shape models and the assumption of ho-
mogeneous thermal properties throughout the surface can still
reproduce the IR data well (see Figs. A.1–A.20, third panel from
the top).

4.2. Constant thermal inertia with temperature

Given the dependence of conductivity on temperature, thermal
inertia obtained from IR data taken at an average heliocentric
distance r needs to be normalised to some reference heliocentric
distance (i.e. temperature), usually 1 au, following

$$\Gamma_{1au} = \Gamma(r)r^{\alpha}, \tag{1}$$

where $\alpha = -0.75$ if we consider a radiative conduction term in
the thermal conductivity κ. Marsset et al. (2017) analysed ther-
mal IR data of asteroid (6) Hebe taken at a wide range of helio-
centric distances and found indications that higher thermal in-
ertias fitted low-r data better. However, even though our sample
includes some highly eccentric asteroids, our OMR versus helio-
centric distance plots show no systematics or biases due to the
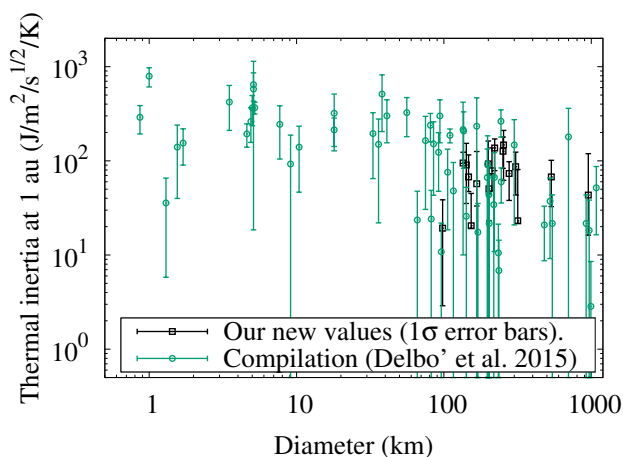
Fig. 1. Thermal inertia normalised at 1 au versus size. The PACS targets (black symbols) follow the trend in the compilation by Delbo' et al. and Hanuš et al. (2018b).
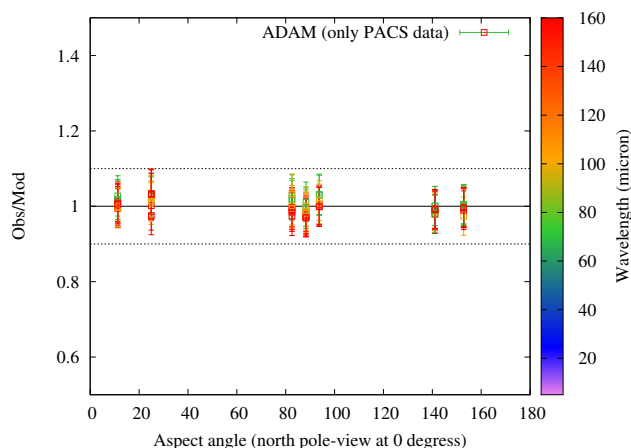
Fig. 2. Observation to model ratios vs. aspect angle for the best fitting TPM model to the PACS data of (2) Pallas. The best fit was obtained by $\Gamma = 30 \, \mathrm{J\,m^{-2}\,s^{-1/2}K^{-1}}$ and a re-scaling of 1.03 (see Table 2).

Fig. 3. Same as Fig. 2 but for the case when we kept the scale of the ADAM model fixed. Here, the best-fitting thermal inertia was 8 $\mathrm{J\,m^{-2}\,s^{-1/2}K^{-1}}$(cf. 30 $\mathrm{J\,m^{-2}\,s^{-1/2}K^{-1}}$), but the data taken with a sub-observer point far from the equator could not be reproduced equally well.

Fig. 4. Observation to model ratios vs. phase angle for the best fit to PACS data of (2) Pallas keeping the scale of the shape model fixed. A lower Γ fitted the data better than when the scale was optimised (cf. Fig. A.2, lower panel).

assumption that Γ = constant (see e.g. Fig. 5), so it seems that the temperature range covered by most MBAs might be such that this effect is not critical.

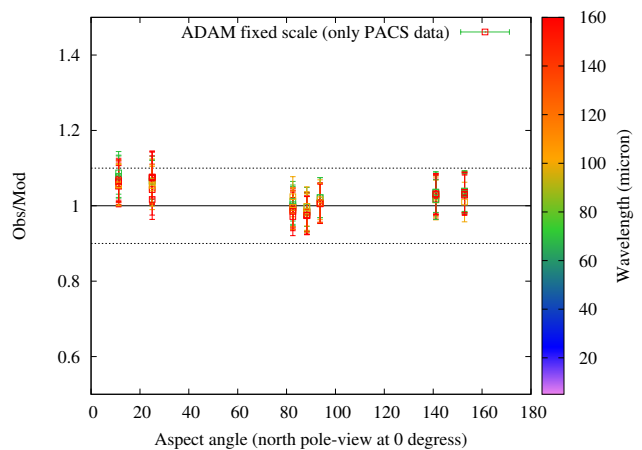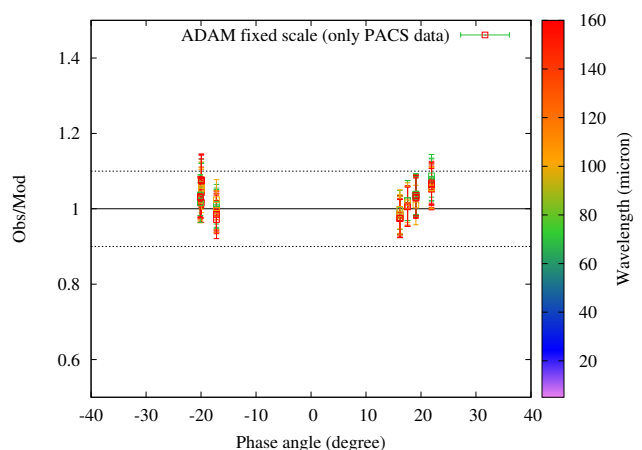Rozitis et al. (2018) studied three highly eccentric near-Earth objects observed by WISE at widely different r and fitted the exponent α separately for each case. This work clearly showed that the physical interpretation of thermal inertia and the comparison between different objects and populations without good constraints for α is quite complicated. Here we propose a graphic approach to analyse a large catalogue of thermal inertias with the necessary assumption that all asteroids can be modelled using a single value of α, which is arguable. The aim, nonetheless is to further explore the impact of the value of this parameter on our interpretation of the thermal inertias with a larger catalogue of values (see also Szakáts et al. 2020).

Instead of normalising the Γ-values to 1 au, we can plot the thermal inertias compiled in Delbo et al. (2015) plus those in Hanuš et al. (2015), Hanuš et al. (2018a), Hanuš et al. (2018b), Marciniak et al. (2018), and Marciniak et al. (2019) as a function of heliocentric distance and compare them with different curves with $\Gamma_{1au} = 10, 50, \ldots, 2000$ and a given value of α using Eq. 1. With such a plot, we can visually estimate Γ_{1au} for each asteroid as the curve going through its corresponding point.

On the one hand, $\alpha = -0.75$ (Fig. 6) leads to the conclusion that most $D > 10$-km asteroids (i.e. the green, brown and yellow symbols) have thermal inertias at 1 au between 10 and 250 $\mathrm{J\,m^{-2}\,s^{-1/2}K^{-1}}$(dotted line), whereas those of most sub-km objects (pink symbols) lie between ~200 and 1000 $\mathrm{J\,m^{-2}\,s^{-1/2}K^{-1}}$. On the other hand, with $\alpha = -2.2$ (Fig. 7), we would conclude that there is a much higher degree of thermal inertia variability amongst $D > 10$ km asteroids, since Γ_{1au} spans the range < 50–2000 $\mathrm{J\,m^{-2}\,s^{-1/2}K^{-1}}$.

Finally, we also examined plots like Figs. 6 and 7 but using the rotational period instead of size in the colour axis: they do not show any appreciable excess of slow rotators in the regions of higher Γ_{1au} or, conversely, fast rotators in the regions with lower Γ_{1au}, regardless of the value of α. This is consistent with the conclusions of Marciniak et al. (2019), whose sample shows that slow rotators do not always present higher thermal inertias (cf. Marciniak et al. 2018, who had a smaller sample, and Harris & Drube 2016 based on an empirical relation between thermal inertia and the infrared beaming parameter η used in the near-Earth asteroid thermal model of Harris 1998).
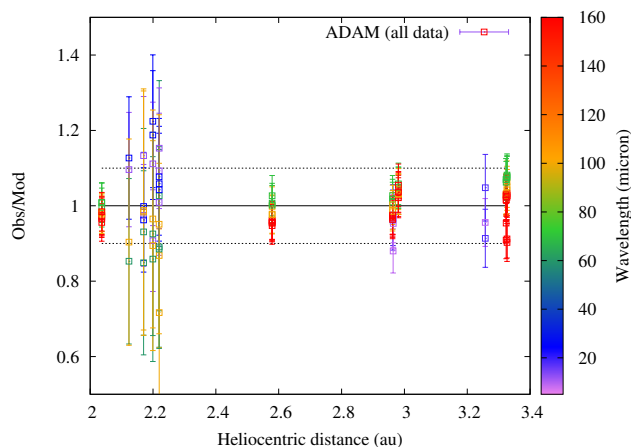
Fig. 5. Observation-to-model ratios vs. heliocentric distance for (3) Juno using the ADAM model. Although there is a slight curvature in the plot, it shows that with reasonable accuracy we can fit data taken at different temperatures with a constant thermal inertia. The more scattered points at about 2.2 au are IRAS data, which did not have a strong weight on the fit given their significantly larger error bars. Section A.3 provides further discussion.

5. Discussion

One of the original motivations for this work within the framework of the SBNAF project was to test how the TPM could be used to evaluate the quality of shape models. While the comparison of the results with those obtained for a sphere is always a useful benchmark for discussion of bad or borderline acceptable fits, we found a relatively small systematic offset of the equivalent diameters obtained for the spherical models. However, after a thorough examination of each individual case, we failed to identify any cause that could explain why the spheres would occasionally provide good approximations of the thermal inertia, while being up to an order of magnitude higher in other cases. Neither the irregularity of the shape nor the particular orientation of the spin axis seem to produce worse results, at least within our sample.

We fully neglect the uncertainties in the shape models even though they would certainly contribute to the final error bars of our TPM parameters (see Hanuš et al. 2015). In this sense, our error bars are lower limits. One of the reasons for this limitation is that the methods to estimate errors in the shape are either labour intensive, computationally costly, or both, but there are already some works that explore this direction. Hanus et al. (2015) proposed a way to assess the effects of shape uncertainty in TPM modelling by bootstrapping the visible data used to obtain a shape model from light-curve inversion and producing a set of shape models, each one of which is in turn modelled with a TPM to provide statistics for the inferred TPM parameters. More recently Bartczak & Dudziński (2019) used an approach featuring millions of slightly perturbed shape clones to examine how the uncertainties and inaccuracies of the inversion models map over the whole surface. As the number of shape models determined from adaptive optics observations and stellar occultations continues to rise, we could reach a point where we have sufficient ground-truth information about the shapes to have a more empirical estimate of the errors of thermal inertia and diameter. Podlewska-Gaca et al. (2020) provide a larger sample of SAGE models scaled with stellar occultation chords and, whenever possible, thermo-physical modelling.

Finally, we note that our thermal inertias for Ceres and Pallas are higher than previous values (Müller & Lagerros 1998; see also Secs. A.1 and A.2). Thermo-physical modelling of Uranian satellites by Detre et al. (submitted to Astronomy & Astrophysics) suggests this could be a small systematic trend: the radiometric diameters are 3-5% larger than the ones derived from direct methods. We have not identified a clear unique cause for such an offset, but it could be related to the absolute flux calibration of the PACS data. On the other hand, we obtained only slightly higher values than O'Rourke et al. (2012) for Lutetia and Capria et al. (2014) for Vesta. Another source of error might be the assumption of a constant emissivity of 0.9, but the need for much lower thermal emissivities has so far been pointed out at significantly longer wavelengths (Müller & Lagerros 1998, Müller & Barnes 2007, Müller et al. 2014).

6. Conclusions

In this work we derive thermo-physical properties of 18 large main-belt asteroids, 12 of which did not have any previous constraints on thermal inertia. This was enabled by previously unpublished Herschel PACS data (Table B) and recently available state-of-the art non-convex shape models (the term also includes the rotational properties). Most of our targets' shape models (see Table 1) were derived from a combination of adaptive optics, occultation and optical light-curve data using the ADAM algorithm (Viikinkoski et al. 2015); three of them, which we used as benchmarks, from direct images from spacecraft, and two of them from only optical light curves via SAGE (Bartczak & Dudziński 2018).

We find that the ADAM shapes can reproduce the thermal IR data in spite of the usual simplifying assumptions of the thermo-physical modelling – constant properties over the surface, and thermal inertia also independent of depth and temperature[5]– even in the case of (10) Hygiea, which has been recently shown to have a variable albedo over the surface (Vernazza et al. 2019). We optimised the scale of the shape models (i.e. the scale was a free parameter in our thermo-physical model, as usual) and found that most cases required an average re-scaling of 5%, which serves as a cross-validation. Nonetheless, there were notable exceptions, especially (65) Cybele (see Table 2), that require ~10% scaling, which means these targets are interesting for follow-up observations and modelling.

From the example of (2) Pallas, a target extensively observed at a wide range of aspect angles due to the high obliquity of its rotation axis, we also examined how potential inaccuracies in the shape can bias the results of thermo-physical modelling when the scale of the shape model is not allowed to vary, so we suggest that results from both approaches (fixed and fitted scale) should always be compared and a careful examination of the modelling results should be performed on a case-by-case basis. Also, more work is needed to quantify and parameterise shape model errors (Hanuš et al. 2015; Bartczak & Dudziński 2019) so that they can be propagated into the thermo-physical properties derived from them in a practical way.

In addition, we found relatively low thermal inertias in the same range as previous results (Delbo et al. 2015, and references therein) for similarly-sized asteroids, which continues to support the notion that these bodies are covered by fine regolith. This, rather than composition, is the dominant effect governing the thermal emission of the large asteroids. Although the peak of

---

[5] A discussion of the case of (6) Hebe can be found in Marsset et al. (2017)
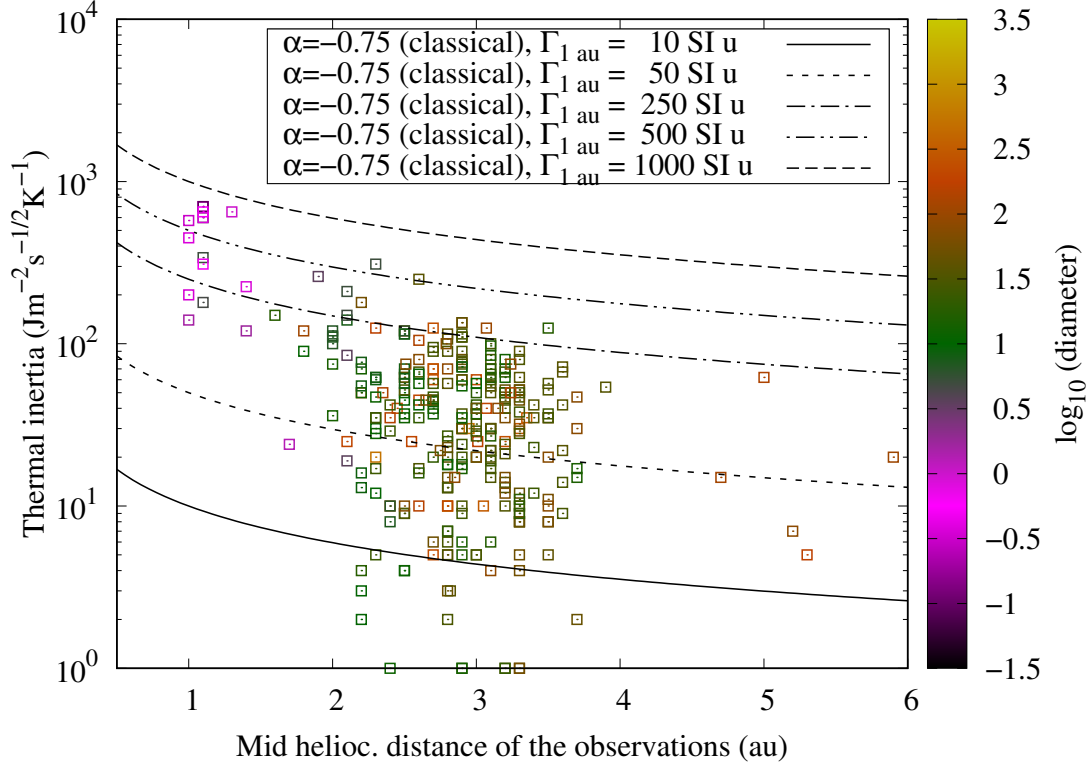
Fig. 6. Thermal inertia vs. average heliocentric distance. We include values compiled from the literature (references given in the text). The lines correspond to Eq. 1 using different values of $\Gamma_{1\,au}$ and the classically assumed $\alpha = -0.75$.
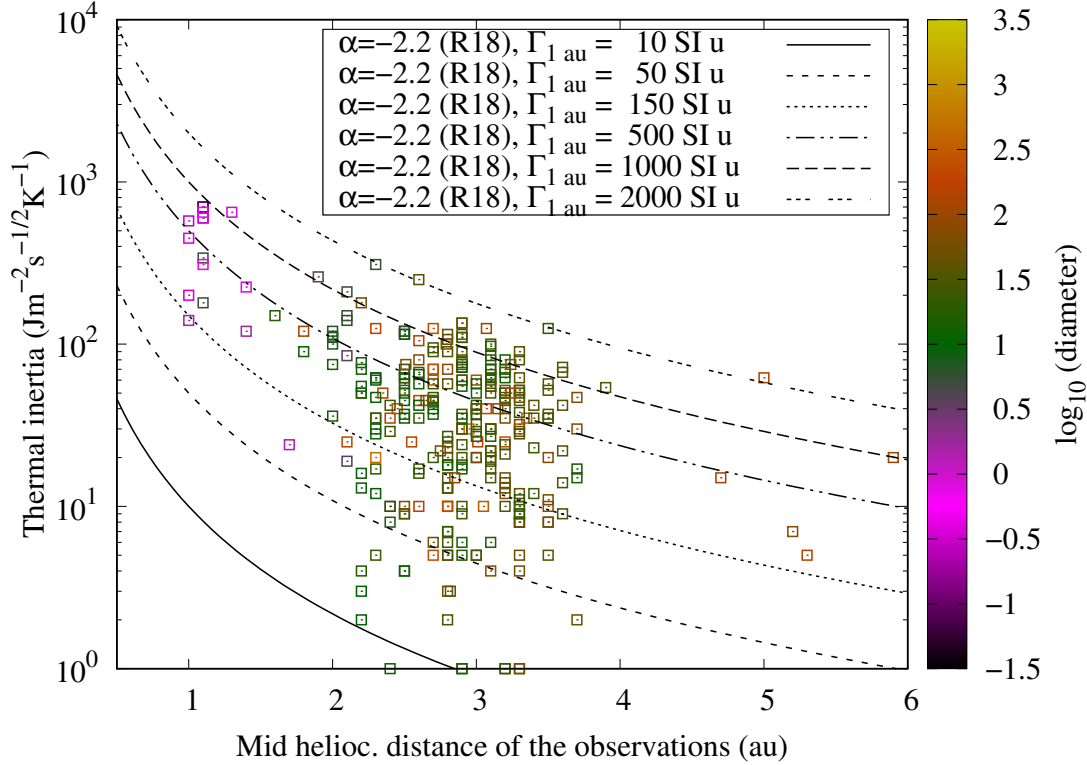
Fig. 7. Same as Fig. 6 but $\alpha = -2.2$, which was found for near-Earth asteroid (1036) Ganymed by Rozitis et al. (2018).

the emission of main-belt asteroids is closer to the 10-micron region of the spectrum, high-quality data at longer wavelengths like PACS data are also extremely useful to determine good-quality sizes and thermal inertias; objects with large data sets especially benefit from the fact that surface roughness is not as dominant as thermal inertia at this wavelength range.

Table 2. Summary of TPM results. D_0 is the sphere-equivalent diameter of the ADAM or in-situ shape models. Spherical model refers to a sphere (∼3000 facets) with the same spin axis. The symbols D, Γ (SI units = J m^{-2} s$^{-1/2}$K^{-1}) and ρ denote the best-fitting diameter, thermal inertia and surface roughness (rms) of the corresponding model. To normalise Γ at 1 au (Γ_{1au}), we took the mid-point ($\bar{r}$) between the shortest and longest heliocentric distance at which the data were taken. The surface roughness (rms) were not constrained at the 1σ level unless otherwise stated. For more information we refer to Appendix A and Table A.1.

Asteroid	Model	D_0 (km)	D (km)	Γ (SI units)	ρ (rms)	$\bar{\chi}^2_m$	$\bar{r}$ (au)	Γ_{1au} (SI units)	Comments
(1) Ceres	Dawn SPC	939.5	951^{+9}_{-7}	25^{+15}_{-10}	∼1	0.2	2.80	43	Modelled PACS data only
	Spherical model		949^{+20}_{-13}	25^{+35}_{-10}		0.5			Similar conclusion but larger error bars
(2) Pallas	ADAM	520	536^{+5}_{-5}	30^{+15}_{-15}	∼0.65	0.4	2.95	67	AKARI data show a small slope in the OMR vs. λ plot
	Spherical model	–	545^{+3}_{-4}	50^{+15}_{-15}		0.6			D ∼5% larger than ADAM → higher Γ
(3) Juno	ADAM	248	252^{+2}_{-3}	60^{+25}_{-20}	∼1	0.5	2.70	126	Feature in the OMR-vs-aspect angle plot
	Spherical model	–	255^{+3}_{-3}	80^{+20}_{-30}		1.0			Formally acceptable fit, consistent thermal properties
	SAGE	–	254^{+3}_{-4}	70^{+30}_{-40}	∼1	1.27		147	Formally acceptable fit, consistent thermal properties
(4) Vesta	Gaskell	522	520^{+12}_{-6}	35^{+55}_{-23}	∼0.9	0.8	2.36	66	Shallow χ^2 minimum, slope in the OMR-vs-wavelength plot
	Spherical model	–	520^{+21}_{-9}	70^{+70}_{-45}		1.1			Formally acceptable fit
(8) Flora	ADAM	143	142^{+2}_{-2}	50^{+35}_{-30}	∼0.4	0.4	2.20	90	IRAS data: slope in the OMR vs. λ plot
	Spherical model	–	147^{+2}_{-1}	120^{+40}_{-40}		0.5			Low χ^2 too, but significantly higher Γ
(10) Hygiea	ADAM	433.6	441^{+7}_{-4}	50^{+20}_{-25}	∼0.9	0.6	3.02	114	IRAS data: slope in the OMR vs. λ plot. IR insensitive to albedo variegation
	Spherical model	–	445^{+5}_{-6}	55^{+25}_{-25}		0.65			Virtually the same results
(18) Melpomene	ADAM	146	135^{+4}_{-1}	50^{+15}_{-44}	∼1	0.3	2.35	95	Shallow and asymmetric χ^2_m. Requires 8% rescaling
	Spherical model	–	143^{+2}_{-1}	80^{+30}_{-40}		0.3			Similar fit, but only small rescaling required (2%)
(19) Fortuna	ADAM	212	219^{+3}_{-2}	40^{+15}_{-15}	∼0.50	0.5	2.45	78	rms>0.2 at 3σ level. Few data but low pole obliquity
	Spherical model	–	219^{+2}_{-9}	20^{+45}_{-5}		1.1			Lower Γ, formally acceptable fit
(20) Massalia	SAGE1	–	147^{+2}_{-2}	35^{+25}_{-10}	∼0.2	0.45	2.40	67	No mirror solution can be rejected. Very low roughness favoured
	Spherical model	–	146	35		1.6			χ^2_m too high, although in agreement with the SAGE results
(21) Lutetia	Jorda	98.15	98^{+1}_{-1}	10^{+10}_{-2}	∼0.6	0.7	2.40	20	0.4 <rms< 0.9. Possible rotational phase shift (see Sect.A.4)
	Spherical model		104	60		> 3			Spherical approximation fails
(29) Amphitrite	ADAM	205.5	202^{+3}_{-2}	25^{+10}_{-13}	∼0.4	0.4	2.55	50	IRAS data: strong slope in the OMR vs. λ plot
	Spherical model		208^{+3}_{-3}	100^{+40}_{-50}		0.9			Formally acceptable fit but significantly higher Γ
(52) Europa	ADAM	313.7	317^{+4}_{-3}	10^{+25}_{-10}	∼0.5	0.5	3.05	23	Very shallow χ^2_m, despite large dataset. $\Gamma \propto T$ effect?
	Spherical model	–	342	200		> 2			Sphere greatly overestimates diameter and Γ
(54) Alexandra	ADAM	143.	153^{+2}_{-2}	10^{+22}_{-10}	∼0.3	0.2	2.60	20	Few data, Southern hemisphere not well sampled in the IR data
	Spherical model	–	161^{+4}_{-3}	75^{+30}_{-45}		0.8			Formally acceptable fit, but inconsistent Γ
(65) Cybele	ADAM	313.3	277^{+4}_{-2}	30^{+10}_{-15}	∼0.45	0.7	3.30	73	Required 12% rescaling. Southern hemisphere not well sampled in the IR
	Spherical model		292^{+5}_{-6}	50^{+20}_{-15}		1.1			Formally acceptable fit, size in better agreement with ADAM
(88) Thisbe	ADAM	220	221^{+2}_{-2}	60^{+15}_{-25}	∼0.9	0.3	3.00	137	IRAS data: slight slope in the OMR vs. λ plot
	Spherical model		219^{+3}_{-2}	60^{+15}_{-35}		0.5			Very low χ^2_m and similar D-Γ despite irregular shape
(93) Minerva	ADAM	160	167^{+3}_{-3}	25^{+30}_{-10}	∼0.2	0.5	3.01	57	Removed MSX and IRAS 12-μm data from analysis
	Spherical model		162^{+2}_{-2}	100^{+10}_{-40}		0.2			Sphere gets lower χ^2_m, but too high Γ
(423) Diotima	ADAM	209	200^{+3}_{-4}	40^{+30}_{-20}	∼0.45	0.6	3.07	93	IRAS data: slope in the OMR vs. λ plot. Southern hemisph. not sampled
	Spherical model		205	150		> 2			Bad fit
(511) Davida	ADAM	313	307^{+7}_{-4}	35^{+15}_{-17}	∼0.5	0.4	3.35	87	IRAS data: slight slope in the OMR vs. λ plot. North. Hemisph. not sampled
	Spherical model		328^{+10}_{-7}	120^{+80}_{-50}		0.6			Low χ^2_m but unrealistically high Γ, perhaps because shape is elongated

References

Alí-Lagoa, V., Delbo', M., & Libourel, G. 2015, ApJ, 810, L22

Alí-Lagoa, V., Lionni, L., Delbo, M., et al. 2014, A&A, 561, A45

Alí-Lagoa, V., Müller, T. G., Usui, F., & Hasegawa, S. 2018, A&A, 612, A85

Bach, Y. P., Ishiguro, M., & Usui, F. 2017, AJ, 154, 202

Balog, Z., Müller, T., Nielbock, M., et al. 2014, Experimental Astronomy, 37, 129

Bartczak, P. & Dudziński, G. 2018, MNRAS, 473, 5050

Bartczak, P. & Dudziński, G. 2019, MNRAS, 485, 2431

Bartczak, P., Michałowski, T., Santana-Ros, T., & Dudziński, G. 2014, MNRAS, 443, 1802

Benner, L. A. M., Busch, M. W., Giorgini, J. D., Taylor, P. A., & Margot, J.-L. 2015, Radar Observations of Near-Earth and Main-Belt Asteroids, ed. P. Michel, F. E. DeMeo, & W. F. Bottke, 165–182

Capria, M. T., Tosi, F., De Sanctis, M. C., et al. 2014, Geophys. Res. Lett., 41, 1438

Carry, B., Dumas, C., Kaasalainen, M., et al. 2010, Icarus, 205, 460

Delbo', M., Dell'Oro, A., Harris, A. W., Mottola, S., & Mueller, M. 2007, Icarus, 190, 236

Delbo, M., Mueller, M., Emery, J. P., Rozitis, B., & Capria, M. T. 2015, Asteroid Thermophysical Modeling, ed. P. Michel, F. E. DeMeo, & W. F. Bottke, 107–128

Delbo', M. & Tanga, P. 2009, Planet. Space Sci., 57, 259

Ďurech, J., Carry, B., Delbo, M., Kaasalainen, M., & Viikinkoski, M. 2015, Asteroid Models from Multiple Data Sources, ed. P. Michel, F. E. DeMeo, & W. F. Bottke, 183–202

Ďurech, J., Delbo', M., Carry, B., Hanuš, J., & Alí-Lagoa, V. 2017, A&A, 604, A27

Ďurech, J., Kaasalainen, M., Herald, D., et al. 2011, Icarus, 214, 652

Ďurech, J., Sidorin, V., & Kaasalainen, M. 2010, A&A, 513, A46

Emery, J. P., Cruikshank, D. P., & Van Cleve, J. 2006, Icarus, 182, 496

Farnham, T. L. 2013, NASA Planetary Data System, ROSETTA SCIENCE ARCHIVE

Hanuš, J., Delbo', M., Alí-Lagoa, V., et al. 2018a, Icarus, 299, 84

Hanuš, J., Delbo', M., Ďurech, J., & Alí-Lagoa, V. 2015, Icarus, 256, 101

Hanuš, J., Delbo', M., Ďurech, J., & Alí-Lagoa, V. 2018b, Icarus, 309, 297

Hanuš, J., Ďurech, J., Brož, M., et al. 2013, A&A, 551, A67

Hanuš, J., Ďurech, J., Brož, M., et al. 2011, A&A, 530, A134

Hanuš, J., Ďurech, J., Oszkiewicz, D. A., et al. 2016, A&A, 586, A108

Hanuš, J., Viikinkoski, M., Marchis, F., et al. 2017, A&A, 601, A114

Harris, A. W. 1998, Icarus, 131, 291

Harris, A. W. & Drube, L. 2016, ApJ, 832, 127

Hasegawa, S., Müller, T. G., Kuroda, D., Takita, S., & Usui, F. 2013, PASJ, 65, 34

Hayne, P. O., Bandfield, J. L., Siegler, M. A., et al. 2017, Journal of Geophysical Research (Planets), 122, 2371

Kaasalainen, M., Mottola, S., & Fulchignoni, M. 2002, Asteroids III, 139

Kaasalainen, M. & Torppa, J. 2001, Icarus, 153, 24

Kaasalainen, M., Torppa, J., & Muinonen, K. 2001, Icarus, 153, 37

Kiss, C., Müller, T. G., Vilenius, E., et al. 2014, Experimental Astronomy, 37, 161

Lagerros, J. S. V. 1996, A&A, 310, 1011

Lagerros, J. S. V. 1998, A&A, 332, 1123

Landsman, Z. A., Emery, J. P., Campins, H., et al. 2018, Icarus, 304, 58

Mainzer, A., Grav, T., Bauer, J., et al. 2011, ApJ, 743, 156

Mainzer, A., Usui, F., & Trilling, D. E. 2015, Space-Based Thermal Infrared Studies of Asteroids, ed. P. Michel, F. E. DeMeo, & W. F. Bottke, 89–106

Mainzer, A. K., Bauer, J. M., Cutri, R. M., et al. 2016, NASA Planetary Data System, 247

Marciniak, A., Alí-Lagoa, V., Müller, T. G., et al. 2019, A&A, 625, A139

Marciniak, A., Bartczak, P., Müller, T., et al. 2018, A&A, 610, A7

Marciniak, A., Bartczak, P., Santana-Ros, T., et al. 2012, A&A, 545, A131

Marsset, M., Carry, B., Dumas, C., et al. 2017, A&A, 604, A64

Masiero, J. R., Mainzer, A. K., Grav, T., et al. 2011, ApJ, 741, 68

Müller, T., Balog, Z., Nielbock, M., et al. 2014, Experimental Astronomy, 37, 253

Müller, T. G. 2002, Meteoritics and Planetary Science, 37, 1919

Müller, T. G. & Barnes, P. J. 2007, A&A, 467, 737

Müller, T. G. & Blommaert, J. A. D. L. 2004, A&A, 418, 347

Müller, T. G., Herschel Calibration Steering Group, & ASTRO-F Calibration Team. 2005a, in ESA Special Publication, Vol. 577, ESA Special Publication, ed. A. Wilson, 471–472

Müller, T. G. & Lagerros, J. S. V. 1998, A&A, 338, 340

Müller, T. G., Marciniak, A., Kiss, C., et al. 2018, Advances in Space Research, 62, 2326

Müller, T. G., Sekiguchi, T., Kaasalainen, M., Abe, M., & Hasegawa, S. 2005b, A&A, 443, 347

Müller, T. G., Ďurech, J., Ishiguro, M., et al. 2017, A&A, 599, A103

Murakami, H., Baba, H., Barthel, P., et al. 2007, PASJ, 59, S369

Nielbock, M., Müller, T., Klaas, U., et al. 2013, Experimental Astronomy, 36, 631

O'Rourke, L., Müller, T., Valtchanov, I., et al. 2012, Planet. Space Sci., 66, 192

Oszkiewicz, D. A., Muinonen, K., Bowell, E., et al. 2011, J. Quant. Spectr. Rad. Transf., 112, 1919

Park, R. S., Vaughan, A. T., Konopliv, A. S., et al. 2019, Icarus, 319, 812

Pilbratt, G. L., Riedinger, J. R., Passvogel, T., et al. 2010, A&A, 518, L1

Podlewska-Gaca, E., Marciniak, A., Alí-Lagoa, V., et al. 2020, arXiv e-prints, arXiv:2001.07030

Poglitsch, A., Waelkens, C., Geis, N., et al. 2010, A&A, 518, L2

Rognini, E. 2018, in COSPAR Meeting, Vol. 42, 42nd COSPAR Scientific Assembly, B1.1–67–18

Rozitis, B. & Green, S. F. 2013, MNRAS, 433, 603

Rozitis, B., Green, S. F., MacLennan, E., & Emery, J. P. 2018, MNRAS, 477, 1782

Rozitis, B., Maclennan, E., & Emery, J. P. 2014, Nature, 512, 174

Szakáts, R., Müller, T., Alí-Lagoa, V., et al. 2020, arXiv e-prints, arXiv:2001.01482

Takita, S., Ikeda, N., Kitamura, Y., et al. 2012, PASJ, 64, 126

Tedesco, E. F., Egan, M. P., & Price, S. D. 2002a, AJ, 124, 583

Tedesco, E. F., Noah, P. V., Noah, M., & Price, S. D. 2002b, AJ, 123, 1056

Usui, F., Kuroda, D., Müller, T. G., et al. 2011, PASJ, 63, 1117

Ďurech, J., Hanuš, J., & Alí-Lagoa, V. 2018, A&A, 617, A57

Vereš, P., Jedicke, R., Fitzsimmons, A., et al. 2015, Icarus, 261, 34

Vernazza, P., Jorda, L., Ševeček, P., et al. 2019, Nature Astronomy, 477

Viikinkoski, M., Hanuš, J., Kaasalainen, M., Marchis, F., & Ďurech, J. 2017, A&A, 607, A117

Viikinkoski, M., Kaasalainen, M., & Durech, J. 2015, A&A, 576, A8

Wright, E. L., Eisenhardt, P. R. M., Mainzer, A. K., et al. 2010, AJ, 140, 1868

Appendix A: Thermo-physical model analysis

In this section we provide all observation-to-model ratio (OMR) plots to help further examine the fits. Table A.1 links each target to its corresponding plots. Some targets warrant a short subsection with relevant comments in addition to those of Table 2.

Table A.1. List of targets and references to the corresponding figures.

Target	OMR plots
(1) Ceres	Fig. A.1
(2) Pallas	Fig. A.2
(3) Juno	Figs. A.3 and A.4
(4) Vesta	Fig. A.5
(8) Flora	Fig. A.6
(10) Hygiea	Fig. A.7
(18) Melpomene	Fig. A.8
(19) Fortuna	Fig. A.9
(20) Massalia	Fig. A.10
(21) Lutetia	Fig. A.12
(29) Amphitrite	Fig. A.13
(52) Europa	Fig. A.14
(54) Alexandra	Fig. A.15
(65) Cybele	Fig. A.16
(88) Thisbe	Fig. A.17
(93) Minerva	Fig. A.18
(423) Diotima	Fig. A.19
(511) Davida	Fig. A.20

Appendix A.1: (1) Ceres

The 180 PACS data points are fitted with a very low $\bar{\chi}^2_{\min}$ of 0.2 with $\Gamma = 25\,\mathrm{J\,m^{-2}\,s^{-1/2}K^{-1}}$, an extremely high roughness of rms~1, and a rescaling of about +2% of the original ADAM shape. This thermal inertia is higher than but compatible within the error bars with classical TPM results ($10 \pm 10\,\mathrm{J\,m^{-2}\,s^{-1/2}K^{-1}}$; Müller & Lagerros 1998) and Dawn-based analyses ($< 20\,\mathrm{J\,m^{-2}\,s^{-1/2}K^{-1}}$; Rognini 2018). If we fit the data while keeping the Dawn stereo-photoclinometry (SPC) shape fixed, we obtain a lower thermal inertia of $6^{+9}_{-6}\,\mathrm{J\,m^{-2}\,s^{-1/2}K^{-1}}$ and roughness values lower than rms~0.35 are rejected at the 3σ level.

We find systematically higher thermal inertias when we model only PACS data and optimise the diameter, although the results are not statistically significantly different (1-σ regions in the χ^2 vs. Γ plots overlap). Actually, for targets with such a rich PACS data set as Ceres, we can fit data from the three PACS filters separately. We found $\Gamma = 35, 40,$ and $50\,\mathrm{J\,m^{-2}\,s^{-1/2}K^{-1}}$ with the 70, 100, and 160 μm data. Although the trend is not statistically significant – our χ^2 minima still overlap within the ranges of formally acceptable fits – it could be caused by the fact that the longer wavelengths probe deeper and perhaps more compacted layers of the subsurface. However, it could also be an artefact related to our assumption of a constant emissivity of 0.9 if the (spectral) emissivity at the PACS wavelengths was lower, but previous work by Müller (2002) suggests that the effect should only be significant at wavelengths much longer than that of PACS. Indeed, Müller et al. (2014) were able to reproduce even Herschel Spectral and Photometric Imaging Receiver (SPIRE) data at 250, 350 and 500 μm with the same modelling approach we use. Nonetheless, we leave it to future work to revisit the data with additional observations and better constraints on spectral emissivity.

Appendix A.2: (2) Pallas

The ADAM shape fits the 80 PACS data with a very low $\bar{\chi}^2_{\min}$ (lower than 0.1) with extremely high roughness and a thermal inertia of $30\,\mathrm{J\,m^{-2}\,s^{-1/2}K^{-1}}$. Nevertheless, we find indications of small shape model inaccuracies given it cannot reproduce all data equally well when we fix the scale (see the main text).

Appendix A.3: (3) Juno

The OMR plots present systematics within the 10% error margins. From the aspect angle plot, we infer that the northern hemisphere part of the shape model could have an artefact, and the wavelength plot shows a slight "convex up" curvature. The SAGE model provides a borderline formally acceptable fit and shows more scatter in the OMR plots and larger parameter error bars, which means the shape is not optimal (the rotational parameters are virtually the same). The trends in the OMR plots are slightly blurred to the eye due to the higher scatter. Nonetheless, the best-fitting values of size and gamma are fully compatible within the error bars, but the ADAM ones are still better constrained. The same can be said about the scatter in the plots corresponding to the sphere (which does slightly better than SAGE in terms of χ^2, but not statistically significantly).

Appendix A.4: (21) Lutetia

For this target we incorporated most of the data featured in O'Rourke et al. (2012) in our analysis, for example Spitzer Infrared Array Camera (IRAC) fluxes, with the notable exception of Herschel SPIRE fluxes, which we did not model in this work. As expected, our results for Lutetia are fully consistent with the previous work. O'Rourke et al. suggest that a localised inaccuracy in the shape model, which is after all based on data that did not cover 100% of Lutetia's surface, is responsible for the inability of the TPM model to fully reproduce the October 17 IRAC thermal light curve (see their Fig. 4). Here we also considered an offset in the rotational zero-phase as a possible explanation, so we repeated the analysis with a delay of 20 degrees. As Fig. A.11 shows, the maxima and minima of the model were better aligned with both IRAC light curves but the overall flux levels of the October 17 one were still not matched. Nevertheless, this mismatch is small, on average 5% (pink OMRs at aspect angle close to 40 degrees in the fourth panel of Fig. A.12), and a possible localised inaccuracy in the shape-model still cannot be ruled out.

Appendix B: Herschel PACS observations

We refer the reader to the caption of Table B.1.
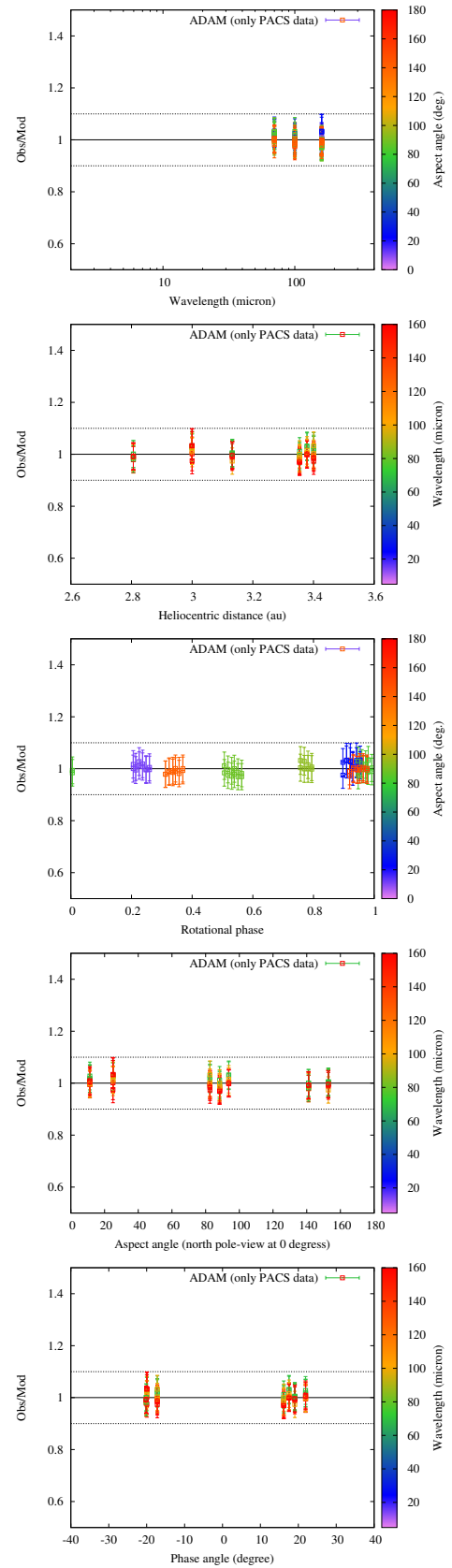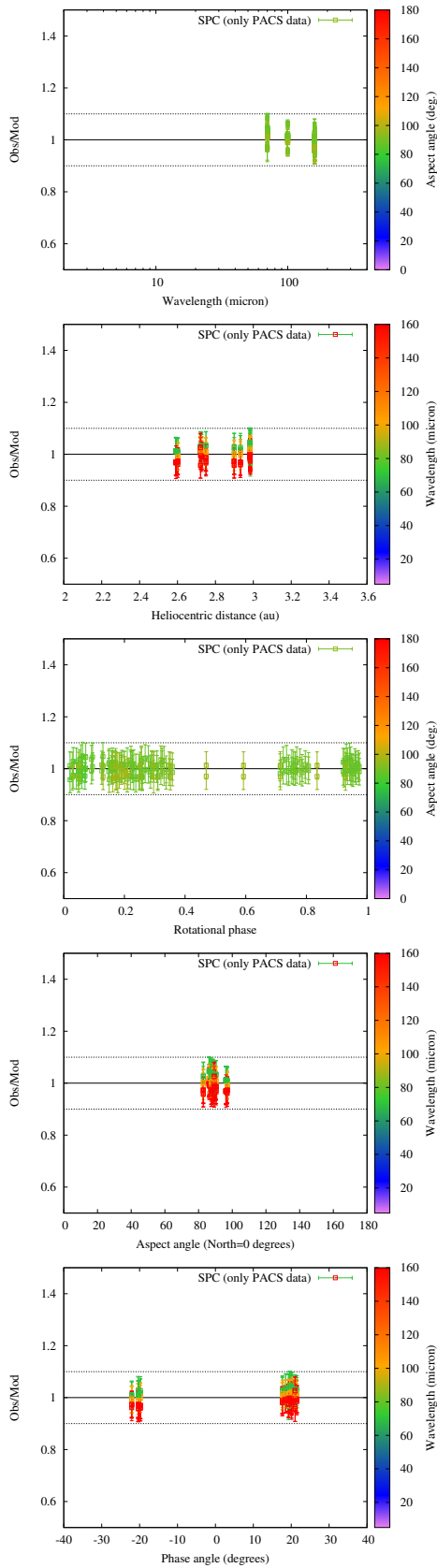
Fig. A.1. (1) Ceres: From top to bottom, observation-to-model ratios vs. wavelength, heliocentric distance, rotational phase, and phase angle. The colour bar corresponds either to the aspect angle or to the wavelength at which each observation was taken.

Fig. A.2. (2) Pallas. See the caption in Fig. A.1.
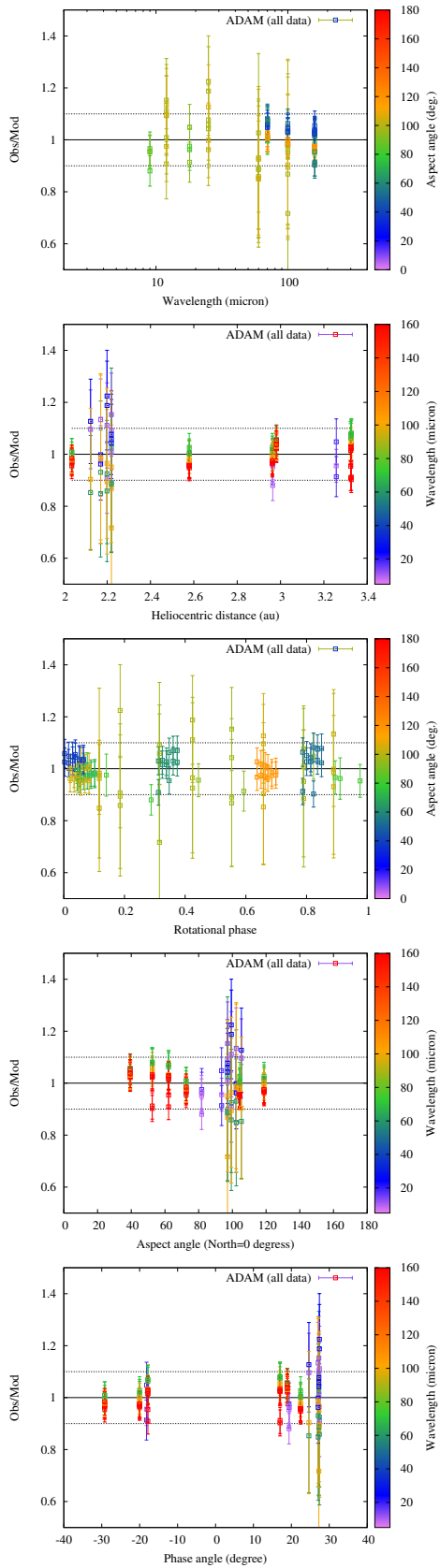
Fig. A.3. (3) Juno (ADAM model). See the caption in Fig. A.1.
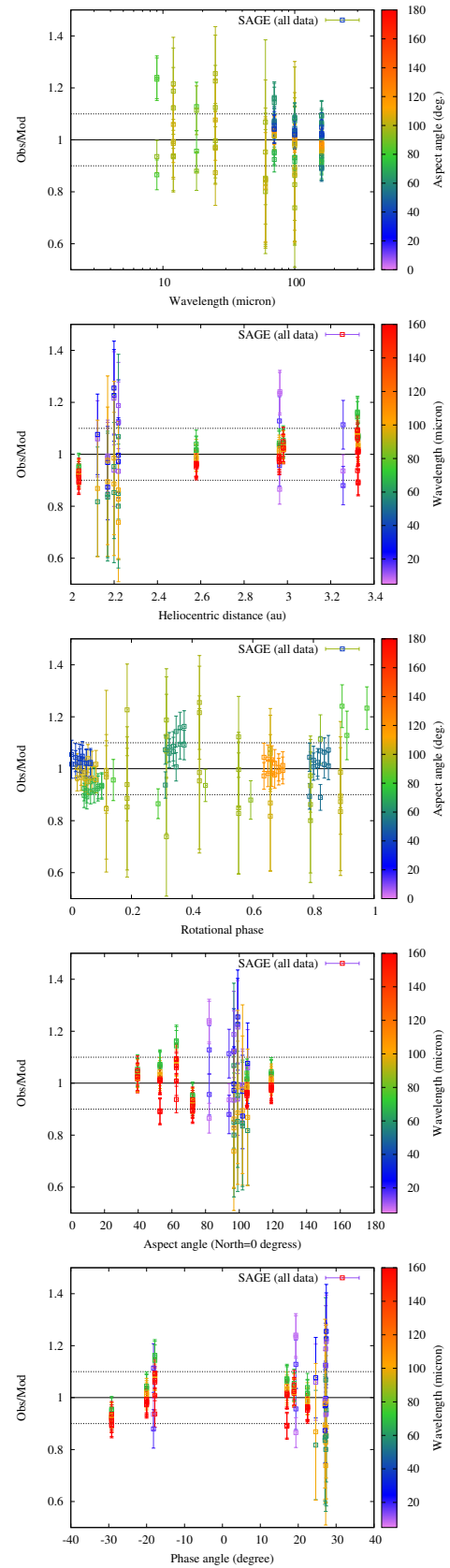
Fig. A.4. (3) Juno (SAGE model). See the caption in Fig. A.1.
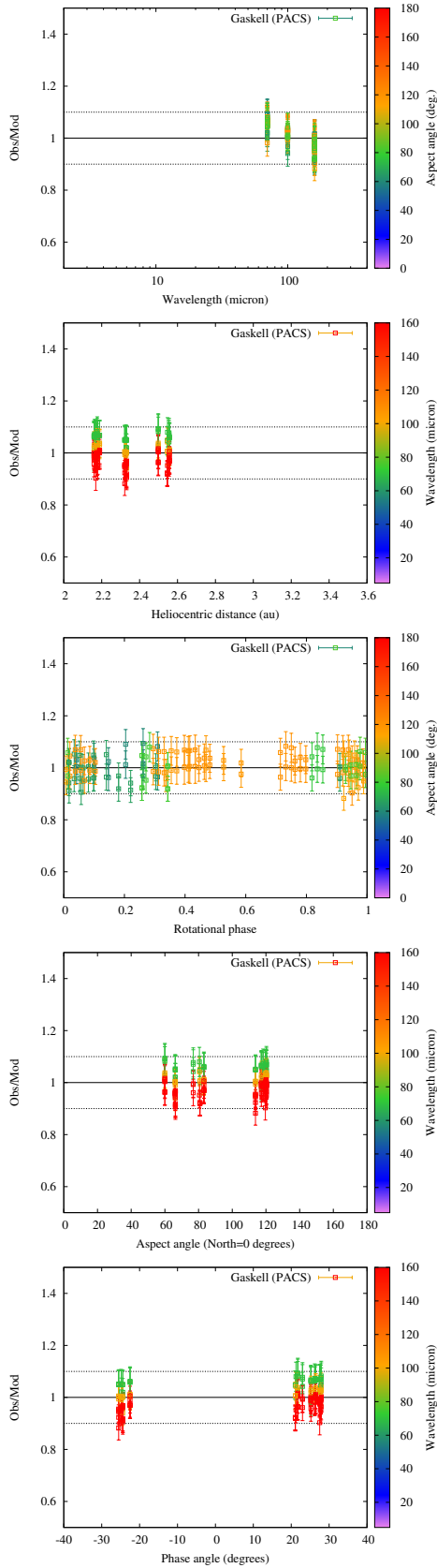
Fig. A.5. (4) Vesta. See the caption in Fig. A.1.
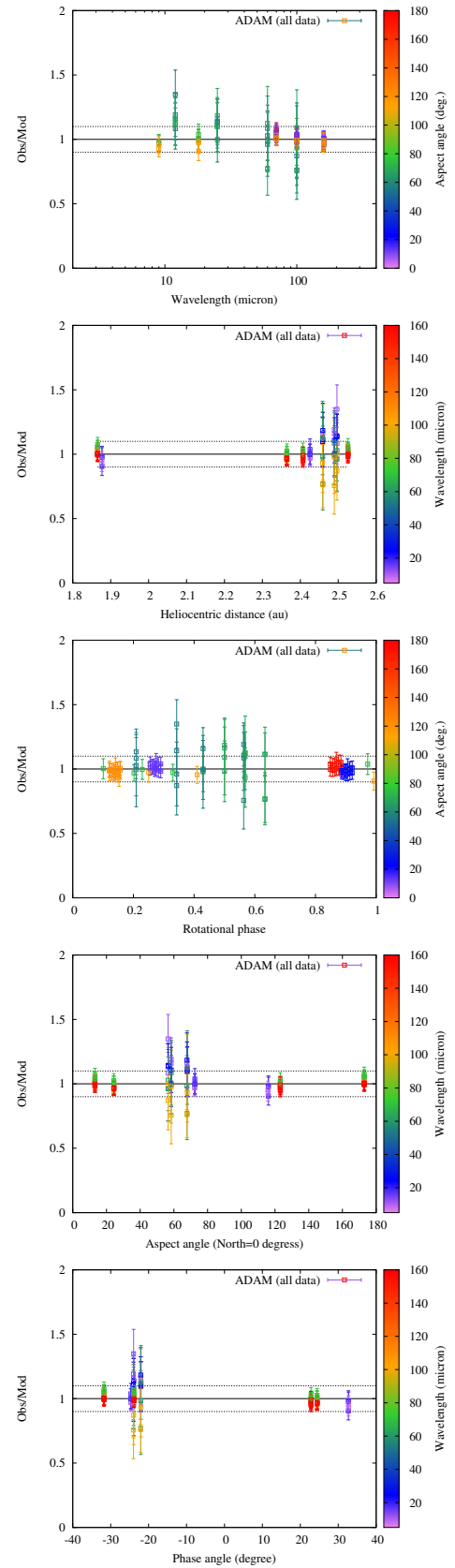
Fig. A.6. (8) Flora. See the caption in Fig. A.1.
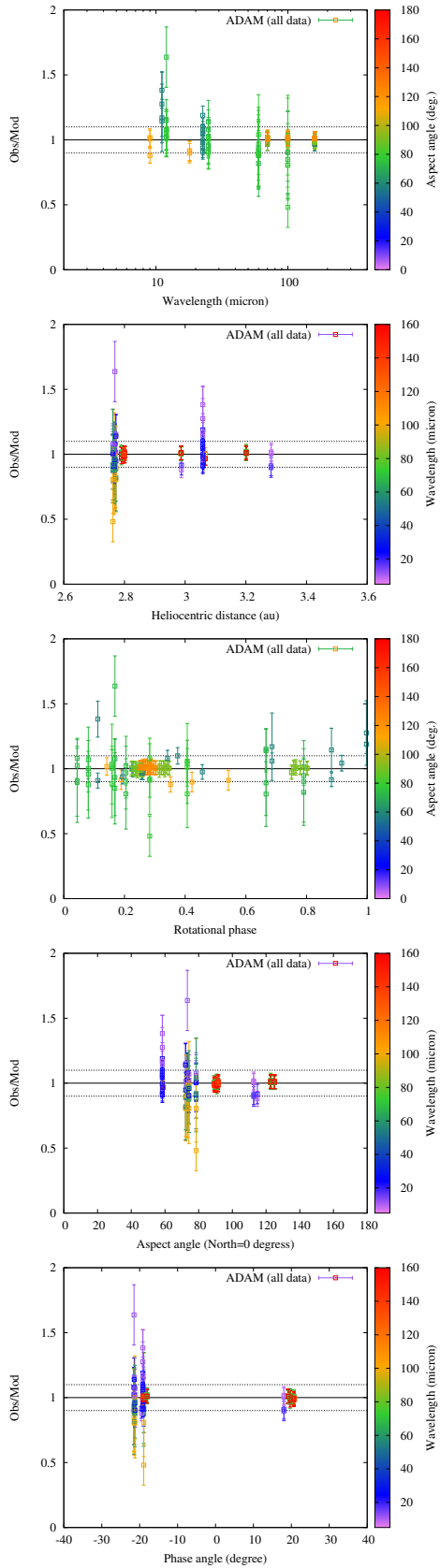
Fig. A.7. (10) Hygiea. See the caption in Fig. A.1.
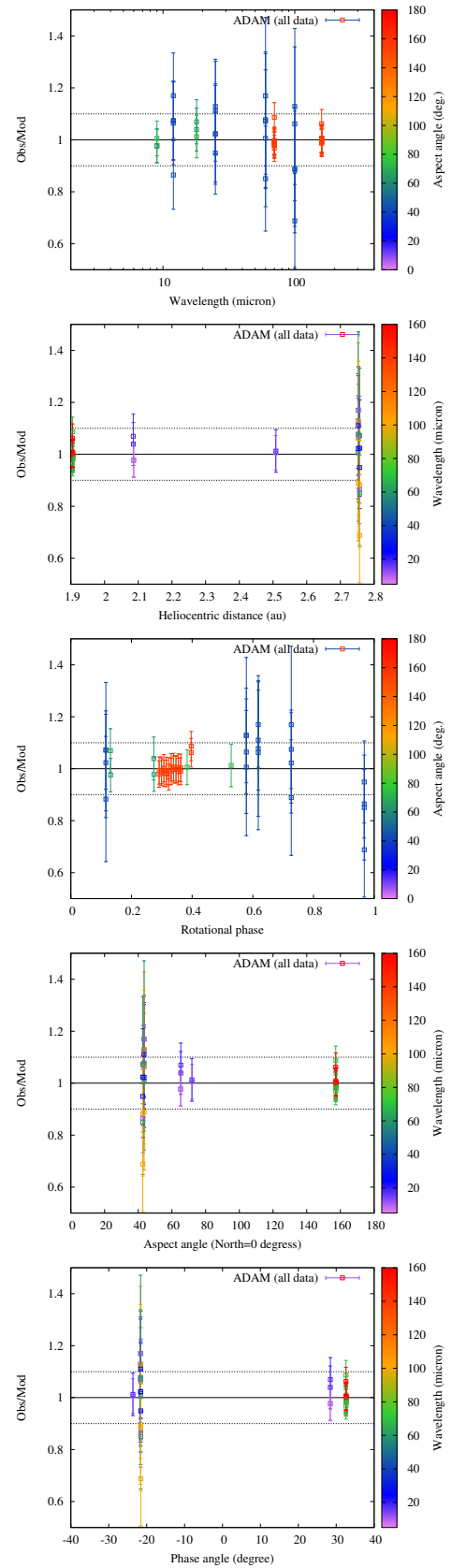
Fig. A.8. (18) Melpomene. See the caption in Fig. A.1.
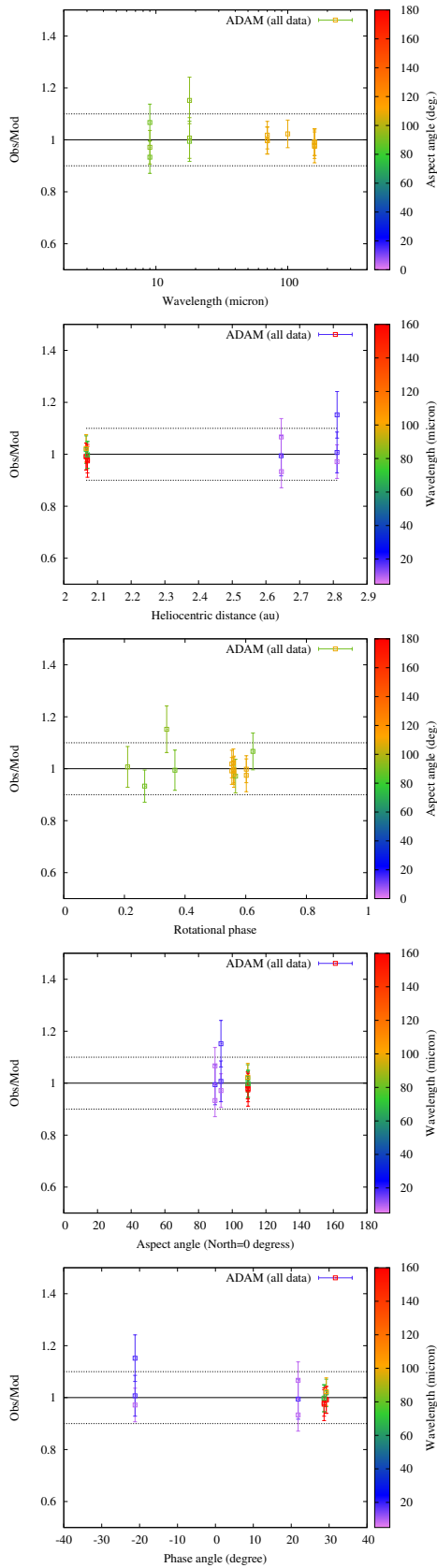
Fig. A.9. (19) Fortuna. See the caption in Fig. A.1.
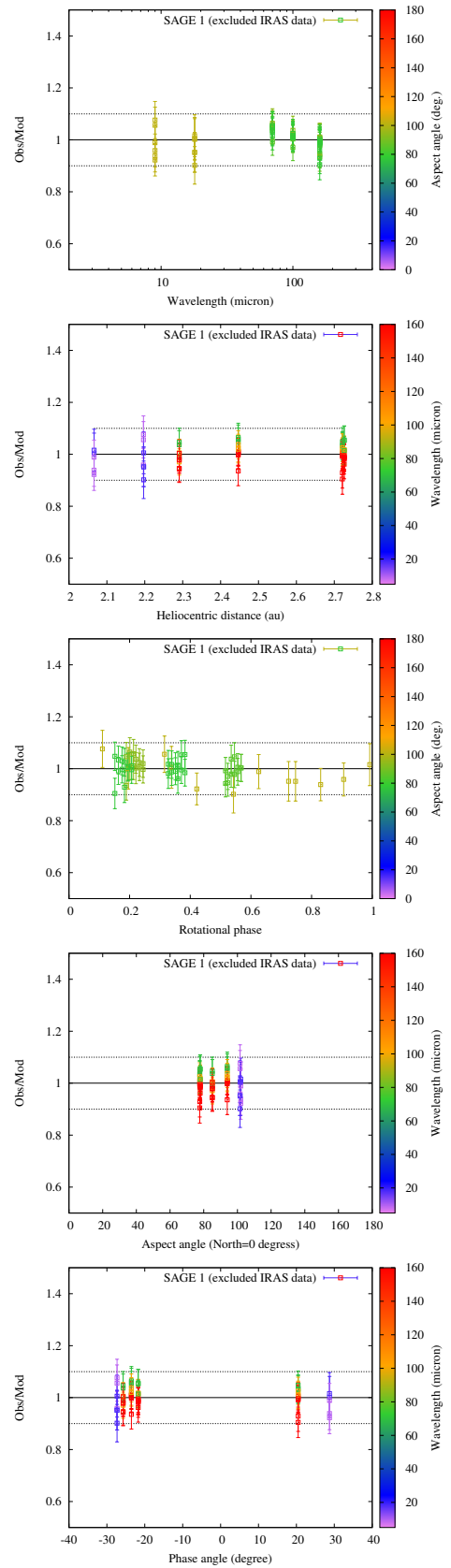
Fig. A.10. (20) Massalia (SAGE model 1). Similar plots were obtained for the second mirror solution.
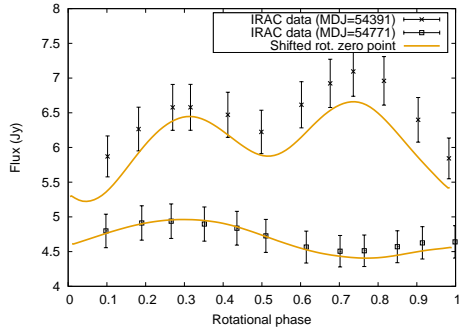
Fig. A.11. Spitzer IRAC thermal light curve of (21) Lutetia ($\lambda = 7.872$ μm) and our best-fitting model fluxes. O'Rourke et al. (2012) provide details of the observations. MDJ is the modified Julian date, the first one (crosses) corresponding to October 17 2007 15:13 UT, the second one (empty squares) to October 31 2008 19:58 UT.
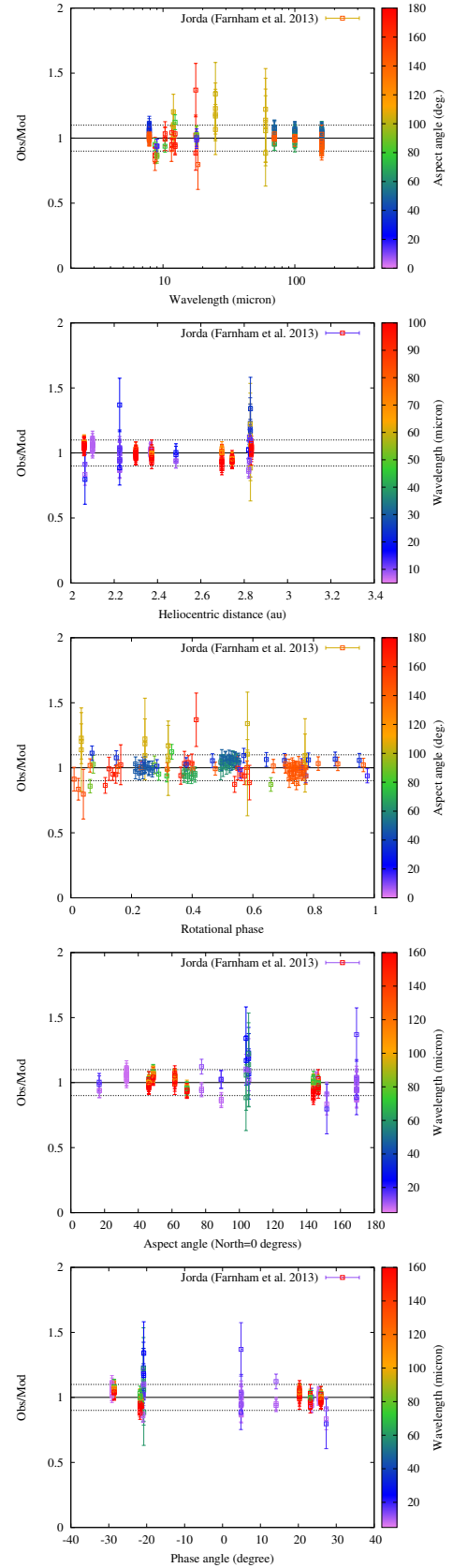
Fig. A.12. (21) Lutetia. See the caption in Fig. A.1.
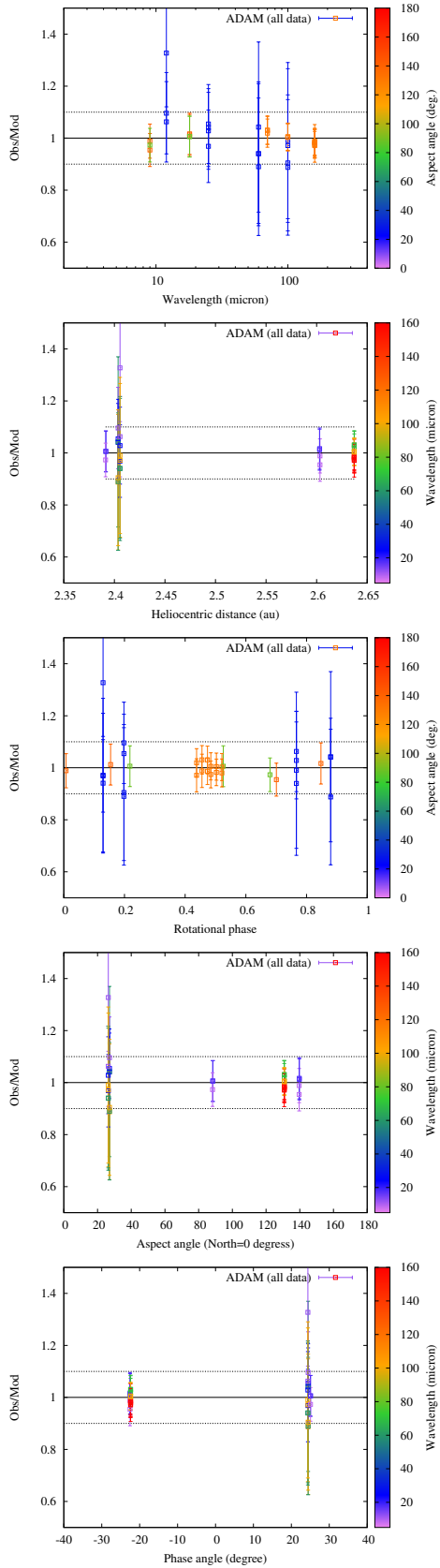
Fig. A.13. (29) Amphitrite. See the caption in Fig. A.1.
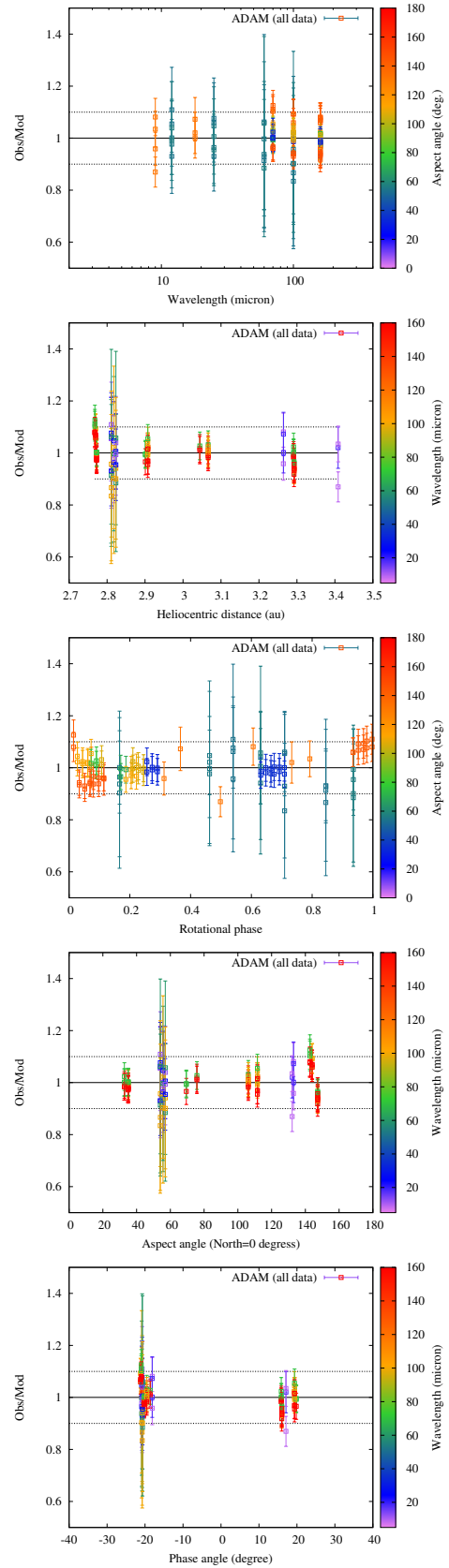
Fig. A.14. (52) Europa. See the caption in Fig. A.1.
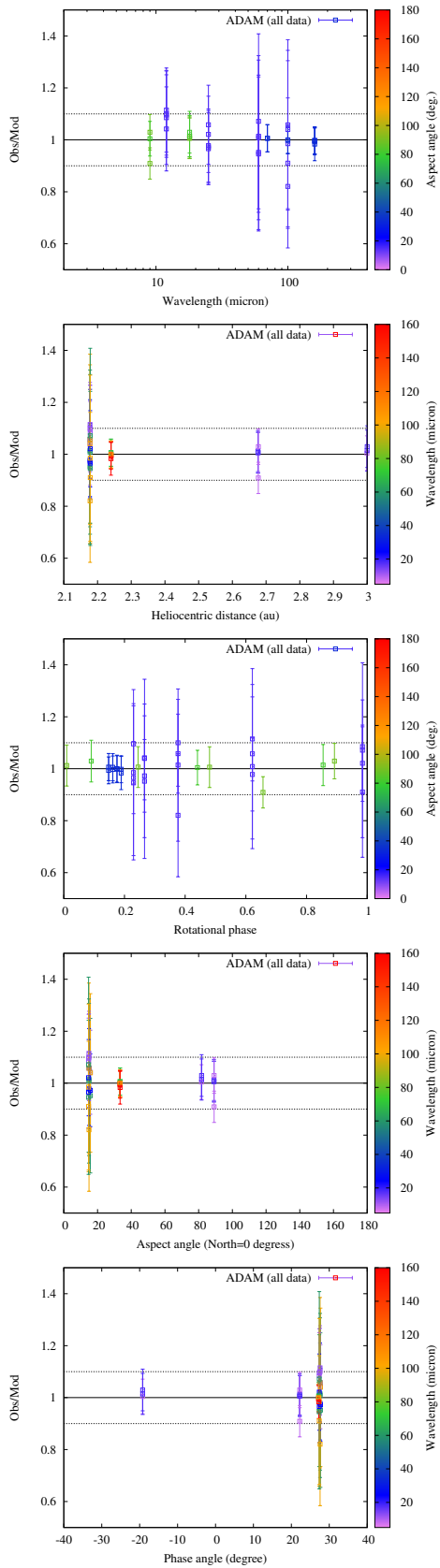
Fig. A.15. (54) Alexandra. See the caption in Fig. A.1.
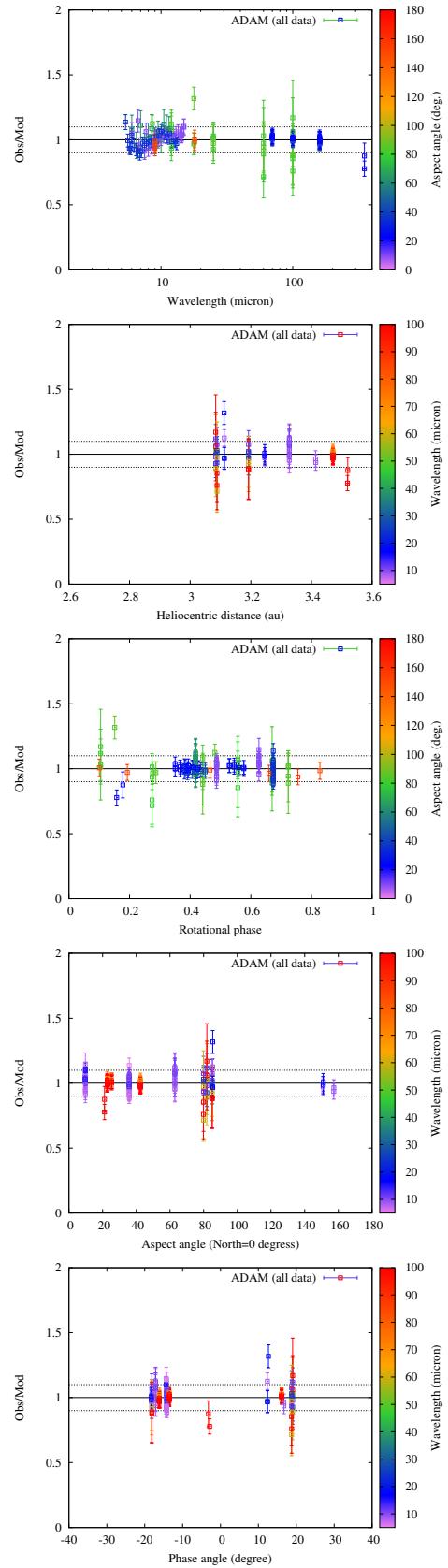
Fig. A.16. (65) Cybele. See the caption in Fig. A.1.
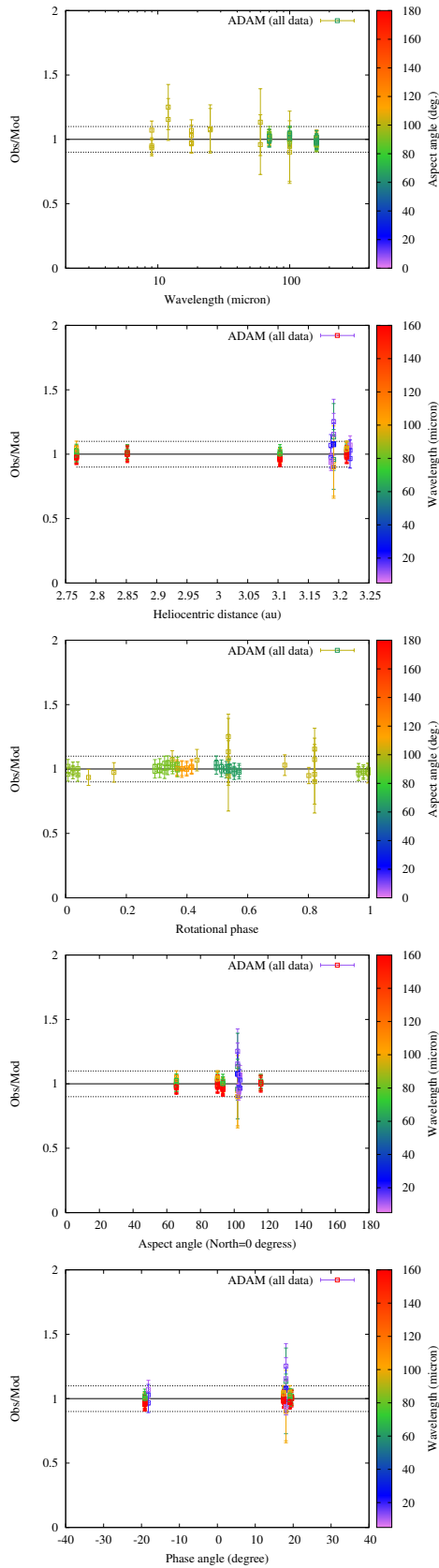
Fig. A.17. (88) Thisbe. See the caption in Fig. A.1.
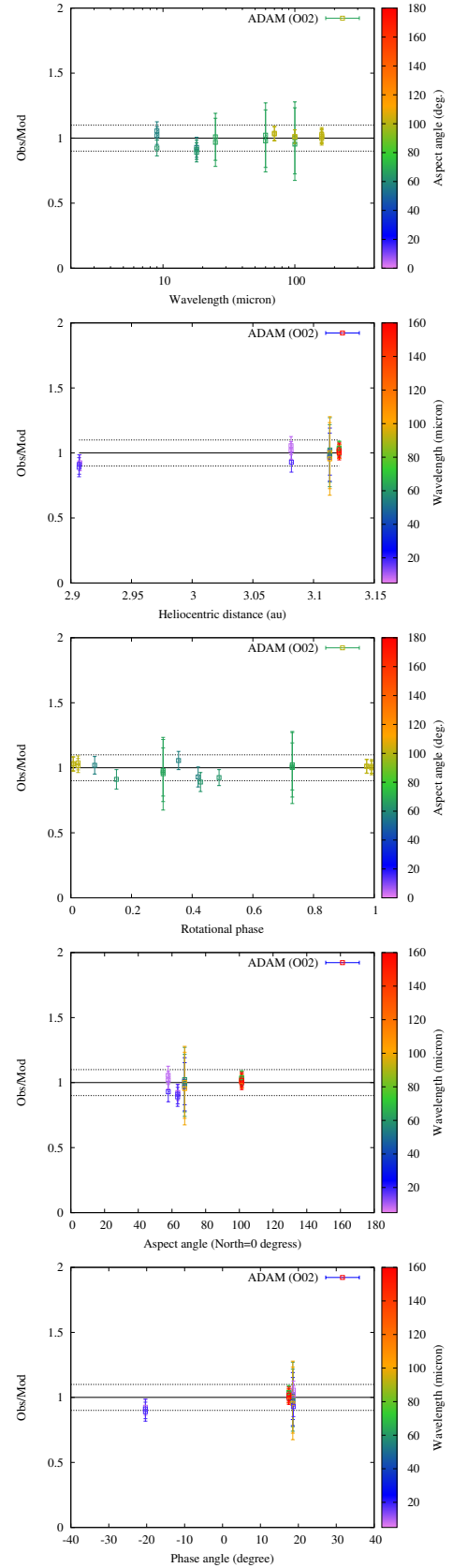
Fig. A.18. (93) Minerva. See the caption in Fig. A.1. Here, O02 is an internal code referring to the best-fitting model to a subset of data. In this case, all MSX observations and 12-micron IRAS data were not modelled because they could not be approximated by any model and they led to extremely high values of thermal inertia and surface roughness.
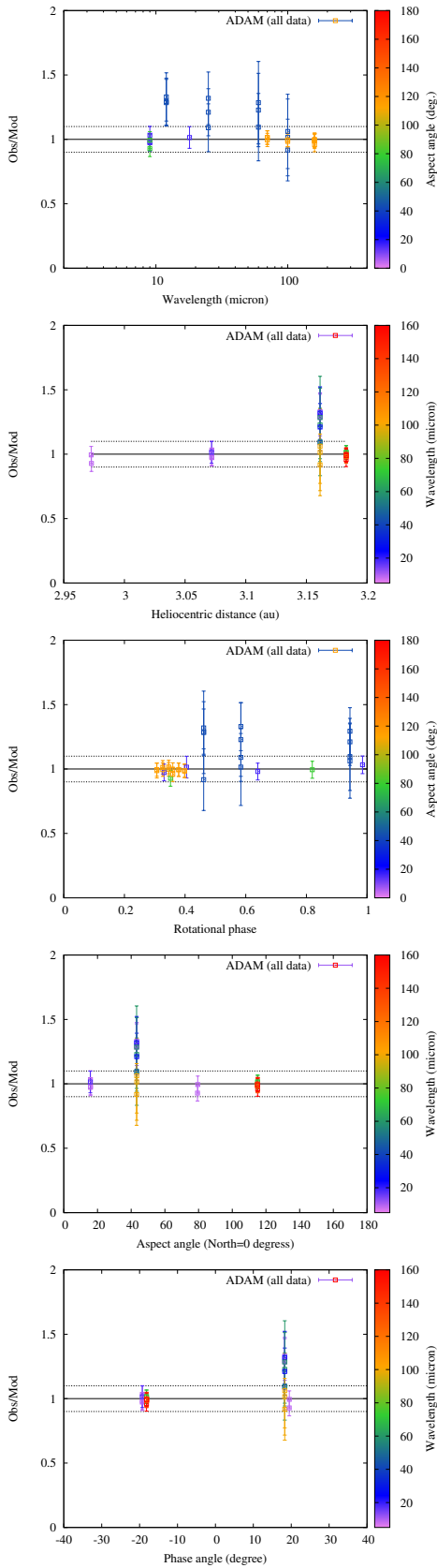
Fig. A.19. (423) Diotima. See the caption in Fig. A.1.
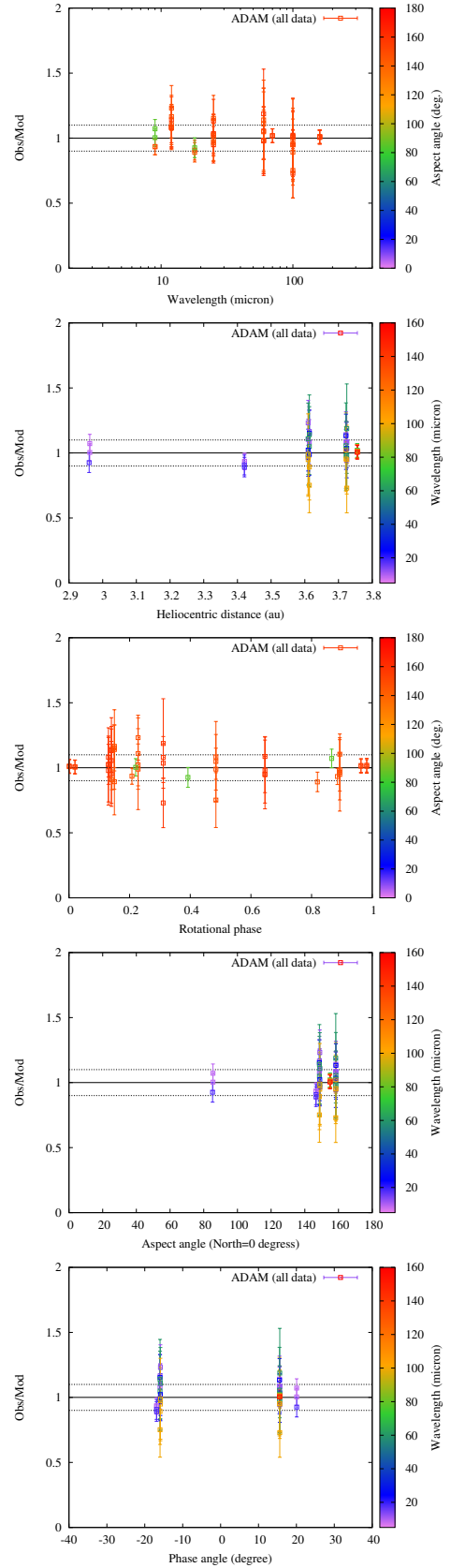
Fig. A.20. (511) Davida. See the caption in Fig. A.1.

Table B.1. Herschel Space Observatory PACS observations used in this work. See Müller et al. (2005b), Nielbock et al. (2013),Balog et al. (2014), and Müller et al. (2014) for details on the data set and observing modes (Obs. mode), and Kiss et al. (2014) on the reduction approach, which required non-standard strategies for a subset of the observations. These fluxes will also be retrievable from the SBNAF database (Szakáts et al. 2020) along with the other data and all relevant references. The start and end times of the observations are denoted by t_s and t_e, λ is the reference wavelength of the band, $\langle f \rangle_\lambda$ and $\sigma \langle f \rangle_\lambda$ the calibrated in-band flux and its error, f_λ the colour-corrected flux density, σf_λ the absolute calibration error, r heliocentric distance, Δ the distance to the observer, and α phase angle. The sign of the phase angle is given by that of the vector product between versors from the asteroid to the Sun and the observer.

Target	Obs. ID	Obs. mode	t_s (JD)	t_e (JD)	Band	$\langle f \rangle_\lambda$ (Jy)	$\langle f \rangle_\lambda$ error (Jy)	λ (μm)	f_λ (Jy)	σf_λ (Jy)	r (au)	Δ (au)	α (deg.)
(3) Juno	1342188358	ChopNod	2455186.74250	2455186.74297	blue	51.7010	0.5174	70	51.444	2.673	2.037	1.765	-29.2
(3) Juno	1342188358	ChopNod	2455186.74250	2455186.74297	red	13.3162	0.1430	160	12.562	0.655	2.037	1.765	-29.2
(3) Juno	1342188359	ChopNod	2455186.74510	2455186.74557	green	29.5331	0.2960	100	28.813	1.497	2.037	1.765	-29.2
(3) Juno	1342188359	ChopNod	2455186.74510	2455186.74557	red	13.1645	0.1415	160	12.419	0.647	2.037	1.765	-29.2
(3) Juno	1342188360	Scanmap	2455186.74776	2455186.75040	blue	52.2075	0.5221	70	51.948	2.699	2.037	1.765	-29.2
(3) Juno	1342188360	Scanmap	2455186.74776	2455186.75040	red	13.3157	0.1338	160	12.562	0.653	2.037	1.765	-29.2
(3) Juno	1342188361	Scanmap	2455186.75143	2455186.75407	blue	51.9514	0.5195	70	51.693	2.686	2.037	1.765	-29.2
(3) Juno	1342188361	Scanmap	2455186.75143	2455186.75407	red	13.2663	0.1333	160	12.515	0.650	2.037	1.765	-29.2
(3) Juno	1342188362	Scanmap	2455186.75510	2455186.75774	green	29.0989	0.2910	100	28.389	1.475	2.037	1.765	-29.2
(3) Juno	1342188362	Scanmap	2455186.75510	2455186.75774	red	13.2155	0.1328	160	12.467	0.648	2.037	1.765	-29.2
(3) Juno	1342188363	Scanmap	2455186.75877	2455186.76140	green	28.6849	0.2869	100	27.985	1.454	2.037	1.765	-29.2
(3) Juno	1342188363	Scanmap	2455186.75877	2455186.76140	red	13.2325	0.1330	160	12.483	0.649	2.037	1.765	-29.2
(3) Juno	1342211811	ChopNod	2455558.62998	2455558.63045	green	17.1489	0.1727	100	16.731	0.870	2.579	2.249	22.4
(3) Juno	1342211811	ChopNod	2455558.62998	2455558.63045	red	7.6438	0.0924	160	7.211	0.378	2.579	2.249	22.4
(3) Juno	1342211812	Scanmap	2455558.63263	2455558.63564	green	16.7354	0.1674	100	16.327	0.848	2.579	2.249	22.4
(3) Juno	1342211812	Scanmap	2455558.63263	2455558.63564	red	7.6058	0.0772	160	7.175	0.373	2.579	2.249	22.4
(3) Juno	1342211813	Scanmap	2455558.63667	2455558.63968	green	16.5611	0.1657	100	16.157	0.840	2.579	2.249	22.4
(3) Juno	1342211813	Scanmap	2455558.63667	2455558.63968	red	7.5155	0.0763	160	7.090	0.369	2.579	2.249	22.4
(3) Juno	1342211814	ChopNod	2455558.64066	2455558.64113	blue	29.6065	0.2968	70	29.459	1.531	2.579	2.249	22.4
(3) Juno	1342211814	ChopNod	2455558.64066	2455558.64113	red	7.4187	0.0906	160	6.999	0.367	2.579	2.249	22.4
(3) Juno	1342211815	Scanmap	2455558.64332	2455558.64632	blue	28.8168	0.2882	70	28.673	1.490	2.579	2.249	22.4
(3) Juno	1342211815	Scanmap	2455558.64332	2455558.64632	red	7.4678	0.0758	160	7.045	0.366	2.579	2.249	22.4
(3) Juno	1342211816	Scanmap	2455558.64736	2455558.65036	blue	28.7475	0.2875	70	28.605	1.486	2.579	2.249	22.4
(3) Juno	1342211816	Scanmap	2455558.64736	2455558.65036	red	7.3943	0.0751	160	6.976	0.363	2.579	2.249	22.4
(3) Juno	1342221855	ChopNod	2455710.81815	2455710.81862	blue	18.8670	0.1898	70	18.773	0.976	2.962	2.637	-20.0
(3) Juno	1342221855	ChopNod	2455710.81815	2455710.81862	red	4.9989	0.0721	160	4.716	0.250	2.962	2.637	-20.0
(3) Juno	1342221856	Scanmap	2455710.82081	2455710.82381	blue	18.5508	0.1856	70	18.459	0.959	2.962	2.637	-20.0
(3) Juno	1342221856	Scanmap	2455710.82081	2455710.82381	red	5.0019	0.0517	160	4.719	0.245	2.962	2.637	-20.0
(3) Juno	1342221857	Scanmap	2455710.82484	2455710.82785	blue	18.3362	0.1834	70	18.245	0.948	2.962	2.637	-20.0
(3) Juno	1342221857	Scanmap	2455710.82484	2455710.82785	red	4.9581	0.0513	160	4.678	0.243	2.962	2.637	-20.0
(3) Juno	1342221858	ChopNod	2455710.82883	2455710.82930	green	10.8492	0.1103	100	10.585	0.550	2.962	2.637	-20.0
(3) Juno	1342221858	ChopNod	2455710.82883	2455710.82930	red	4.9059	0.0715	160	4.628	0.245	2.962	2.637	-20.0
(3) Juno	1342221859	Scanmap	2455710.83149	2455710.83450	green	10.6099	0.1062	100	10.351	0.538	2.962	2.637	-20.0
(3) Juno	1342221859	Scanmap	2455710.83149	2455710.83450	red	4.9400	0.0511	160	4.660	0.242	2.962	2.637	-20.0
(3) Juno	1342221860	Scanmap	2455710.83553	2455710.83854	green	10.6425	0.1065	100	10.383	0.539	2.962	2.638	-20.0
(3) Juno	1342221860	Scanmap	2455710.83553	2455710.83854	red	4.9384	0.0511	160	4.659	0.242	2.962	2.638	-20.0
(3) Juno	1342238893	ChopNod	2455967.40681	2455967.40728	green	6.4966	0.0680	100	6.338	0.330	3.327	3.386	17.0
(3) Juno	1342238893	ChopNod	2455967.40681	2455967.40728	red	2.6352	0.0583	160	2.486	0.138	3.327	3.386	17.0
(3) Juno	1342238894	Scanmap	2455967.40946	2455967.41247	green	6.3771	0.0640	100	6.222	0.323	3.327	3.386	17.0
(3) Juno	1342238894	Scanmap	2455967.40946	2455967.41247	red	2.9479	0.0322	160	2.781	0.145	3.327	3.386	17.0
(3) Juno	1342238895	Scanmap	2455967.41350	2455967.41651	green	6.3012	0.0632	100	6.147	0.320	3.327	3.386	17.0
(3) Juno	1342238895	Scanmap	2455967.41350	2455967.41651	red	2.9349	0.0321	160	2.769	0.144	3.327	3.386	17.0
(3) Juno	1342238896	ChopNod	2455967.41749	2455967.41796	blue	10.8593	0.1106	70	10.805	0.562	3.327	3.386	17.0
(3) Juno	1342238896	ChopNod	2455967.41749	2455967.41796	red	2.5795	0.0580	160	2.433	0.136	3.327	3.386	17.0
(3) Juno	1342238897	Scanmap	2455967.42015	2455967.42315	blue	10.7859	0.1079	70	10.732	0.558	3.327	3.386	17.0

Target	Obs. ID	Obs. mode	t_s (JD)	t_e (JD)	Band	$\langle f \rangle_\lambda$ (Jy)	$\sigma \langle f \rangle_\lambda$ (Jy)	λ (μm)	f_λ (Jy)	σf_λ (Jy)	r (au)	Δ (au)	α (deg.)
(3) Juno	1342238897	Scanmap	2455967.42015	2455967.42315	red	2.9490	0.0322	160	2.782	0.145	3.327	3.386	17.0
(3) Juno	1342238898	Scanmap	2455967.42419	2455967.42719	blue	10.8523	0.1086	70	10.798	0.561	3.327	3.386	17.0
(3) Juno	1342238898	Scanmap	2455967.42419	2455967.42719	red	2.9314	0.0321	160	2.765	0.144	3.327	3.386	17.0
(3) Juno	1342249295	ChopNod	2456149.60314	2456149.60361	green	7.9154	0.0816	100	7.722	0.402	3.324	3.078	-17.8
(3) Juno	1342249295	ChopNod	2456149.60314	2456149.60361	red	3.2891	0.0615	160	3.103	0.169	3.324	3.078	-17.8
(3) Juno	1342249296	Scanmap	2456149.60579	2456149.60880	green	7.9117	0.0793	100	7.719	0.401	3.324	3.078	-17.8
(3) Juno	1342249296	Scanmap	2456149.60579	2456149.60880	red	3.6666	0.0389	160	3.459	0.180	3.324	3.078	-17.8
(3) Juno	1342249297	Scanmap	2456149.60983	2456149.61284	green	7.8602	0.0788	100	7.668	0.399	3.324	3.078	-17.8
(3) Juno	1342249297	Scanmap	2456149.60983	2456149.61284	red	3.6610	0.0388	160	3.454	0.180	3.324	3.078	-17.8
(3) Juno	1342249298	ChopNod	2456149.61382	2456149.61429	blue	13.5514	0.1371	70	13.484	0.701	3.324	3.078	-17.8
(3) Juno	1342249298	ChopNod	2456149.61382	2456149.61429	red	3.4365	0.0623	160	3.242	0.175	3.324	3.078	-17.8
(3) Juno	1342249299	Scanmap	2456149.61648	2456149.61948	blue	13.6383	0.1364	70	13.570	0.705	3.324	3.079	-17.8
(3) Juno	1342249299	Scanmap	2456149.61648	2456149.61948	red	3.7076	0.0393	160	3.498	0.182	3.324	3.079	-17.8
(3) Juno	1342249300	Scanmap	2456149.62052	2456149.62352	blue	13.6492	0.1366	70	13.581	0.706	3.324	3.079	-17.8
(3) Juno	1342249300	Scanmap	2456149.62052	2456149.62352	red	3.6961	0.0392	160	3.487	0.182	3.324	3.079	-17.8
(3) Juno	1342269819	ChopNod	2456393.13257	2456393.13304	blue	16.2571	0.1639	70	16.176	0.841	2.981	3.120	18.9
(3) Juno	1342269819	ChopNod	2456393.13257	2456393.13304	red	4.3142	0.0676	160	4.070	0.217	2.981	3.120	18.9
(3) Juno	1342269820	Scanmap	2456393.13523	2456393.13823	blue	15.9759	0.1598	70	15.896	0.826	2.981	3.120	18.9
(3) Juno	1342269820	Scanmap	2456393.13523	2456393.13823	red	4.2627	0.0446	160	4.021	0.209	2.981	3.120	18.9
(3) Juno	1342269821	Scanmap	2456393.13927	2456393.14227	blue	15.8407	0.1585	70	15.762	0.819	2.981	3.120	18.9
(3) Juno	1342269821	Scanmap	2456393.13927	2456393.14227	red	4.2638	0.0446	160	4.022	0.209	2.981	3.120	18.9
(3) Juno	1342269822	ChopNod	2456393.14325	2456393.14372	green	9.2570	0.0947	100	9.031	0.470	2.981	3.120	18.9
(3) Juno	1342269822	ChopNod	2456393.14325	2456393.14372	red	4.3432	0.0678	160	4.097	0.218	2.981	3.120	18.9
(3) Juno	1342269823	Scanmap	2456393.14591	2456393.14892	green	9.0867	0.0910	100	8.865	0.461	2.981	3.120	18.9
(3) Juno	1342269823	Scanmap	2456393.14591	2456393.14892	red	4.2364	0.0443	160	3.997	0.208	2.981	3.120	18.9
(3) Juno	1342269824	Scanmap	2456393.14995	2456393.15296	green	9.0288	0.0904	100	8.809	0.458	2.981	3.120	18.9
(3) Juno	1342269824	Scanmap	2456393.14995	2456393.15296	red	4.2200	0.0442	160	3.981	0.207	2.981	3.120	18.9
(8) Flora	1342182740	ChopNod	2455066.93796	2455066.93844	blue	6.1766	0.0652	70	6.146	0.320	2.514	2.754	-21.7
(8) Flora	1342182740	ChopNod	2455066.93796	2455066.93844	red	1.6713	0.0546	160	1.577	0.096	2.514	2.754	-21.7
(8) Flora	1342182740	ChopNod	2455066.94178	2455066.94226	blue	6.1504	0.0650	70	6.120	0.319	2.514	2.754	-21.7
(8) Flora	1342182740	ChopNod	2455066.94178	2455066.94226	red	1.6385	0.0545	160	1.546	0.094	2.514	2.754	-21.7
(8) Flora	1342182740	ChopNod	2455066.94560	2455066.94607	blue	6.1592	0.0651	70	6.129	0.319	2.514	2.754	-21.7
(8) Flora	1342182740	ChopNod	2455066.94560	2455066.94607	red	1.6594	0.0546	160	1.565	0.095	2.514	2.754	-21.7
(8) Flora	1342182740	ChopNod	2455066.94942	2455066.94989	blue	6.1750	0.0652	70	6.144	0.320	2.514	2.754	-21.7
(8) Flora	1342182740	ChopNod	2455066.94942	2455066.94989	red	1.7095	0.0547	160	1.613	0.097	2.514	2.754	-21.7
(8) Flora	1342182740	ChopNod	2455066.95324	2455066.95371	blue	6.1962	0.0654	70	6.165	0.321	2.514	2.754	-21.7
(8) Flora	1342182740	ChopNod	2455066.95324	2455066.95371	red	1.7046	0.0547	160	1.608	0.097	2.514	2.754	-21.7
(8) Flora	1342182740	ChopNod	2455066.95706	2455066.95753	blue	6.2185	0.0656	70	6.188	0.322	2.514	2.754	-21.7
(8) Flora	1342182740	ChopNod	2455066.95706	2455066.95753	red	1.7498	0.0549	160	1.651	0.099	2.514	2.754	-21.7
(8) Flora	1342182740	ChopNod	2455066.96088	2455066.96135	blue	6.2339	0.0658	70	6.203	0.323	2.514	2.754	-21.7
(8) Flora	1342182740	ChopNod	2455066.96088	2455066.96135	red	1.7314	0.0548	160	1.633	0.098	2.514	2.754	-21.7
(8) Flora	1342182740	ChopNod	2455066.96470	2455066.96517	blue	6.2627	0.0661	70	6.231	0.325	2.514	2.754	-21.7
(8) Flora	1342182740	ChopNod	2455066.96470	2455066.96517	red	1.6933	0.0547	160	1.597	0.096	2.514	2.754	-21.7
(8) Flora	1342182740	ChopNod	2455066.96852	2455066.96899	blue	6.2397	0.0658	70	6.209	0.323	2.514	2.754	-21.7
(8) Flora	1342182740	ChopNod	2455066.96852	2455066.96899	red	1.7033	0.0547	160	1.607	0.097	2.514	2.754	-21.7
(8) Flora	1342182740	ChopNod	2455066.97234	2455066.97281	blue	6.2860	0.0663	70	6.255	0.326	2.514	2.754	-21.7
(8) Flora	1342182740	ChopNod	2455066.97234	2455066.97281	red	1.7061	0.0547	160	1.609	0.097	2.514	2.754	-21.7
(8) Flora	1342182740	ChopNod	2455066.97616	2455066.97663	blue	6.3377	0.0668	70	6.306	0.328	2.514	2.754	-21.7
(8) Flora	1342182740	ChopNod	2455066.97616	2455066.97663	red	1.6343	0.0545	160	1.542	0.094	2.514	2.754	-21.7

Table B.1. continued.

Target	Obs. ID	Obs. mode	t_s (JD)	t_e (JD)	Band	$\langle f \rangle_\lambda$ (Jy)	$\sigma \langle f \rangle_\lambda$ (Jy)	λ (μm)	f_λ (Jy)	σf_λ (Jy)	r (au)	Δ (au)	α (deg.)
(8) Flora	1342182740	ChopNod	2455066.97998	2455066.98045	blue	6.3695	0.0671	70	6.338	0.330	2.514	2.754	-21.7
(8) Flora	1342182740	ChopNod	2455066.97998	2455066.98045	red	1.6898	0.0547	160	1.594	0.096	2.514	2.754	-21.7
(8) Flora	1342182740	ChopNod	2455066.98380	2455066.98427	blue	6.4189	0.0675	70	6.387	0.333	2.514	2.754	-21.7
(8) Flora	1342182740	ChopNod	2455066.98380	2455066.98427	red	1.6457	0.0545	160	1.552	0.094	2.514	2.754	-21.7
(8) Flora	1342182740	ChopNod	2455066.98762	2455066.98809	blue	6.4396	0.0677	70	6.408	0.334	2.514	2.754	-21.7
(8) Flora	1342182740	ChopNod	2455066.98762	2455066.98809	red	1.6297	0.0545	160	1.538	0.094	2.514	2.754	-21.7
(8) Flora	1342182740	ChopNod	2455066.99144	2455066.99191	blue	6.4403	0.0677	70	6.408	0.334	2.514	2.755	-21.7
(8) Flora	1342182740	ChopNod	2455066.99144	2455066.99191	red	1.5864	0.0544	160	1.497	0.092	2.514	2.755	-21.7
(8) Flora	1342210638	ChopNod	2455531.73973	2455531.74021	green	19.4082	0.1951	100	18.935	0.984	1.866	1.413	-31.8
(8) Flora	1342210638	ChopNod	2455531.73973	2455531.74021	red	8.6829	0.1012	160	8.191	0.428	1.866	1.413	-31.8
(8) Flora	1342210639	Scanmap	2455531.74239	2455531.74540	green	19.3260	0.1933	100	18.855	0.980	1.866	1.413	-31.8
(8) Flora	1342210639	Scanmap	2455531.74239	2455531.74540	red	8.6496	0.0875	160	8.160	0.424	1.866	1.413	-31.8
(8) Flora	1342210640	Scanmap	2455531.74643	2455531.74944	green	19.0954	0.1910	100	18.630	0.968	1.866	1.413	-31.8
(8) Flora	1342210640	Scanmap	2455531.74643	2455531.74944	red	8.6476	0.0874	160	8.158	0.424	1.866	1.413	-31.8
(8) Flora	1342210641	ChopNod	2455531.75042	2455531.75089	blue	34.9219	0.3498	70	34.748	1.806	1.866	1.413	-31.8
(8) Flora	1342210641	ChopNod	2455531.75042	2455531.75089	red	8.6279	0.1007	160	8.139	0.426	1.866	1.413	-31.8
(8) Flora	1342210642	Scanmap	2455531.75307	2455531.75608	blue	34.3522	0.3435	70	34.181	1.776	1.866	1.413	-31.8
(8) Flora	1342210642	Scanmap	2455531.75307	2455531.75608	red	8.6584	0.0876	160	8.168	0.425	1.866	1.413	-31.8
(8) Flora	1342210643	Scanmap	2455531.75711	2455531.76012	blue	34.2017	0.3420	70	34.032	1.768	1.866	1.413	-31.8
(8) Flora	1342210643	Scanmap	2455531.75711	2455531.76012	red	8.6435	0.0874	160	8.154	0.424	1.866	1.413	-31.8
(8) Flora	1342236950	ChopNod	2455934.38240	2455934.38287	green	8.2184	0.0846	100	8.018	0.417	2.365	1.981	24.4
(8) Flora	1342236950	ChopNod	2455934.38240	2455934.38287	red	3.7545	0.0641	160	3.542	0.191	2.365	1.981	24.4
(8) Flora	1342236951	Scanmap	2455934.38505	2455934.38806	green	8.2927	0.0831	100	8.090	0.420	2.365	1.981	24.4
(8) Flora	1342236951	Scanmap	2455934.38505	2455934.38806	red	3.7759	0.0399	160	3.562	0.185	2.365	1.981	24.4
(8) Flora	1342236952	Scanmap	2455934.38909	2455934.39210	green	8.2514	0.0827	100	8.050	0.418	2.365	1.981	24.4
(8) Flora	1342236952	Scanmap	2455934.38909	2455934.39210	red	3.7667	0.0398	160	3.554	0.185	2.365	1.981	24.4
(8) Flora	1342236953	ChopNod	2455934.39308	2455934.39355	blue	14.8185	0.1497	70	14.745	0.766	2.365	1.981	24.4
(8) Flora	1342236953	ChopNod	2455934.39308	2455934.39355	red	3.7481	0.0641	160	3.536	0.190	2.365	1.981	24.4
(8) Flora	1342236954	Scanmap	2455934.39574	2455934.39874	blue	14.5872	0.1459	70	14.515	0.754	2.365	1.981	24.4
(8) Flora	1342236954	Scanmap	2455934.39574	2455934.39874	red	3.7682	0.0399	160	3.555	0.185	2.365	1.981	24.4
(8) Flora	1342236955	Scanmap	2455934.39978	2455934.40278	blue	14.5726	0.1458	70	14.500	0.753	2.365	1.980	24.4
(8) Flora	1342236955	Scanmap	2455934.39978	2455934.40278	red	3.7922	0.0401	160	3.578	0.186	2.365	1.980	24.4
(8) Flora	1342246945	ChopNod	2456089.51768	2456089.51816	green	6.6105	0.0691	100	6.449	0.336	2.525	2.218	-23.9
(8) Flora	1342246945	ChopNod	2456089.51768	2456089.51816	red	2.9327	0.0597	160	2.767	0.152	2.525	2.218	-23.9
(8) Flora	1342246946	Scanmap	2456089.52034	2456089.52335	green	6.5169	0.0654	100	6.358	0.330	2.525	2.218	-23.9
(8) Flora	1342246946	Scanmap	2456089.52034	2456089.52335	red	3.0178	0.0329	160	2.847	0.148	2.525	2.218	-23.9
(8) Flora	1342246947	Scanmap	2456089.52438	2456089.52739	green	6.4885	0.0651	100	6.330	0.329	2.525	2.218	-23.9
(8) Flora	1342246947	Scanmap	2456089.52438	2456089.52739	red	2.9977	0.0327	160	2.828	0.147	2.525	2.218	-23.9
(8) Flora	1342246948	ChopNod	2456089.52837	2456089.52884	blue	11.6244	0.1181	70	11.567	0.601	2.525	2.218	-23.9
(8) Flora	1342246948	ChopNod	2456089.52837	2456089.52884	red	2.9883	0.0600	160	2.819	0.154	2.525	2.218	-23.9
(8) Flora	1342246949	Scanmap	2456089.53103	2456089.53403	blue	11.4300	0.1144	70	11.373	0.591	2.525	2.218	-23.9
(8) Flora	1342246949	Scanmap	2456089.53103	2456089.53403	red	2.9794	0.0325	160	2.811	0.147	2.525	2.218	-23.9
(8) Flora	1342246950	Scanmap	2456089.53506	2456089.53807	blue	11.3862	0.1139	70	11.330	0.589	2.525	2.218	-23.9
(8) Flora	1342246950	Scanmap	2456089.53506	2456089.53807	red	2.9865	0.0326	160	2.817	0.147	2.525	2.218	-23.9
(8) Flora	1342267585	ChopNod	2456366.08142	2456366.08190	green	4.3902	0.0482	100	4.283	0.223	2.407	2.585	22.8
(8) Flora	1342267585	ChopNod	2456366.08142	2456366.08190	red	1.9181	0.0554	160	1.810	0.106	2.407	2.585	22.8
(8) Flora	1342267586	Scanmap	2456366.08408	2456366.08709	green	4.3461	0.0437	100	4.240	0.220	2.407	2.585	22.8
(8) Flora	1342267586	Scanmap	2456366.08408	2456366.08709	red	1.9979	0.0238	160	1.885	0.099	2.407	2.585	22.8
(8) Flora	1342267587	Scanmap	2456366.08812	2456366.09113	green	4.2990	0.0433	100	4.194	0.218	2.407	2.585	22.8

Target	Obs. ID	Obs. mode	t_s (JD)	t_e (JD)	Band	$\langle f \rangle_\lambda$ (Jy)	$\sigma \langle f \rangle_\lambda$ (Jy)	λ (μm)	f_λ (Jy)	σf_λ (Jy)	r (au)	Δ (au)	α (deg.)
(8) Flora	1342267587	Scanmap	2456366.08812	2456366.09113	red	1.9683	0.0236	160	1.857	0.097	2.407	2.585	22.8
(8) Flora	1342267588	ChopNod	2456366.09211	2456366.09258	blue	7.6828	0.0796	70	7.645	0.398	2.407	2.585	22.8
(8) Flora	1342267588	ChopNod	2456366.09211	2456366.09258	red	1.9436	0.0555	160	1.834	0.107	2.407	2.585	22.8
(8) Flora	1342267589	Scanmap	2456366.09476	2456366.09777	blue	7.4917	0.0750	70	7.454	0.387	2.407	2.585	22.8
(8) Flora	1342267589	Scanmap	2456366.09476	2456366.09777	red	1.9745	0.0236	160	1.863	0.098	2.407	2.585	22.8
(8) Flora	1342267590	Scanmap	2456366.09880	2456366.10181	blue	7.4920	0.0750	70	7.455	0.387	2.407	2.585	22.8
(8) Flora	1342267590	Scanmap	2456366.09880	2456366.10181	red	1.9881	0.0238	160	1.876	0.098	2.407	2.585	22.8
(18) Melpomene	1342179011	ChopNod	2455006.65020	2455006.65067	blue	22.2603	0.2236	70	22.150	1.151	1.905	1.622	32.6
(18) Melpomene	1342179011	ChopNod	2455006.65020	2455006.65067	red	5.8551	0.0783	160	5.524	0.291	1.905	1.622	32.6
(18) Melpomene	1342179011	ChopNod	2455006.65402	2455006.65449	blue	22.6012	0.2270	70	22.489	1.169	1.905	1.622	32.6
(18) Melpomene	1342179011	ChopNod	2455006.65402	2455006.65449	red	5.8230	0.0781	160	5.493	0.290	1.905	1.622	32.6
(18) Melpomene	1342179011	ChopNod	2455006.65784	2455006.65831	blue	22.3633	0.2246	70	22.252	1.156	1.905	1.622	32.6
(18) Melpomene	1342179011	ChopNod	2455006.65784	2455006.65831	red	5.9176	0.0788	160	5.583	0.294	1.905	1.622	32.6
(18) Melpomene	1342179011	ChopNod	2455006.66166	2455006.66213	blue	22.4251	0.2252	70	22.314	1.160	1.905	1.622	32.6
(18) Melpomene	1342179011	ChopNod	2455006.66166	2455006.66213	red	5.8772	0.0785	160	5.545	0.292	1.905	1.622	32.6
(18) Melpomene	1342179011	ChopNod	2455006.66548	2455006.66595	blue	22.1298	0.2223	70	22.020	1.144	1.905	1.622	32.6
(18) Melpomene	1342179011	ChopNod	2455006.66548	2455006.66595	red	5.8730	0.0784	160	5.541	0.292	1.905	1.622	32.6
(18) Melpomene	1342179011	ChopNod	2455006.66929	2455006.66977	blue	22.6384	0.2274	70	22.526	1.171	1.905	1.621	32.6
(18) Melpomene	1342179011	ChopNod	2455006.66929	2455006.66977	red	5.9600	0.0791	160	5.623	0.296	1.905	1.621	32.6
(18) Melpomene	1342179011	ChopNod	2455006.67311	2455006.67359	blue	22.6149	0.2271	70	22.502	1.169	1.905	1.621	32.6
(18) Melpomene	1342179011	ChopNod	2455006.67311	2455006.67359	red	5.9243	0.0788	160	5.589	0.294	1.905	1.621	32.6
(18) Melpomene	1342179011	ChopNod	2455006.67693	2455006.67741	blue	22.5810	0.2268	70	22.469	1.168	1.905	1.621	32.6
(18) Melpomene	1342179011	ChopNod	2455006.67693	2455006.67741	red	5.8689	0.0784	160	5.537	0.292	1.905	1.621	32.6
(18) Melpomene	1342179011	ChopNod	2455006.68075	2455006.68123	blue	22.3841	0.2248	70	22.273	1.157	1.905	1.621	32.6
(18) Melpomene	1342179011	ChopNod	2455006.68075	2455006.68123	red	5.8995	0.0786	160	5.566	0.293	1.905	1.621	32.6
(18) Melpomene	1342179011	ChopNod	2455006.68457	2455006.68504	blue	22.5390	0.2264	70	22.427	1.165	1.905	1.621	32.6
(18) Melpomene	1342179011	ChopNod	2455006.68457	2455006.68504	red	5.9170	0.0788	160	5.582	0.294	1.905	1.621	32.6
(18) Melpomene	1342179012	Scanmap	2455006.68920	2455006.71359	blue	24.7791	0.2478	70	24.656	1.281	1.905	1.621	32.6
(18) Melpomene	1342179012	Scanmap	2455006.68920	2455006.71359	red	6.2727	0.0641	160	5.918	0.308	1.905	1.621	32.6
(19) Fortuna	1342183903	ChopNod	2455089.82776	2455089.82823	blue	46.5430	0.4659	70	46.311	2.406	2.066	1.710	29.2
(19) Fortuna	1342183903	ChopNod	2455089.82776	2455089.82823	red	12.0162	0.1309	160	11.336	0.591	2.066	1.710	29.2
(19) Fortuna	1342183904	ChopNod	2455089.83037	2455089.83084	green	27.4459	0.2752	100	26.776	1.391	2.066	1.710	29.2
(19) Fortuna	1342183904	ChopNod	2455089.83037	2455089.83084	red	12.1019	0.1317	160	11.417	0.595	2.066	1.710	29.2
(19) Fortuna	1342184287	Scanmap	2455097.85343	2455097.87429	blue	47.1886	0.4719	70	46.954	2.440	2.070	1.625	28.7
(19) Fortuna	1342184287	Scanmap	2455097.85343	2455097.87428	red	12.4594	0.1253	160	11.754	0.611	2.070	1.625	28.7
(19) Fortuna	1342184288	Scanmap	2455097.87526	2455097.89610	red	13.2821	0.1335	160	12.530	0.651	2.070	1.625	28.7
(19) Fortuna	1342184288	Scanmap	2455097.87526	2455097.89612	blue	50.6065	0.5061	70	50.355	2.616	2.070	1.625	28.7
(20) Massalia	1342188346	ChopNod	2455186.69915	2455186.69963	blue	12.0359	0.1222	70	11.976	0.623	2.291	2.057	-25.7
(20) Massalia	1342188346	ChopNod	2455186.69915	2455186.69963	red	3.1064	0.0606	160	2.931	0.160	2.291	2.057	-25.7
(20) Massalia	1342188347	ChopNod	2455186.70176	2455186.70223	green	6.8973	0.0718	100	6.729	0.350	2.291	2.057	-25.7
(20) Massalia	1342188347	ChopNod	2455186.70176	2455186.70223	red	3.1075	0.0606	160	2.932	0.160	2.291	2.057	-25.7
(20) Massalia	1342188348	Scanmap	2455186.70442	2455186.70705	blue	12.4995	0.1251	70	12.437	0.646	2.291	2.057	-25.7
(20) Massalia	1342188348	Scanmap	2455186.70442	2455186.70705	red	3.2105	0.0346	160	3.029	0.158	2.291	2.057	-25.7
(20) Massalia	1342188349	Scanmap	2455186.70808	2455186.71072	blue	12.5234	0.1253	70	12.461	0.647	2.291	2.057	-25.7
(20) Massalia	1342188349	Scanmap	2455186.70808	2455186.71072	red	3.1789	0.0343	160	2.999	0.156	2.291	2.057	-25.7
(20) Massalia	1342188350	Scanmap	2455186.71175	2455186.71439	green	7.0398	0.0706	100	6.868	0.357	2.291	2.058	-25.7
(20) Massalia	1342188350	Scanmap	2455186.71175	2455186.71439	red	3.2046	0.0346	160	3.023	0.158	2.291	2.058	-25.7
(20) Massalia	1342188351	Scanmap	2455186.71542	2455186.71806	green	6.9535	0.0697	100	6.784	0.352	2.291	2.058	-25.7
(20) Massalia	1342188351	Scanmap	2455186.71542	2455186.71806	red	3.2273	0.0348	160	3.045	0.159	2.291	2.058	-25.7

Table B.1. continued.

Target	Obs. ID	Obs. mode	t_s (JD)	t_e (JD)	Band	$\langle f \rangle_\lambda$ (Jy)	$\sigma\langle f \rangle_\lambda$ (Jy)	λ (μm)	f_λ (Jy)	σf_λ (Jy)	r (au)	Δ (au)	α (deg.)
(20) Massalia	1342224165	ChopNod	2455757.13413	2455757.13460	blue	6.7993	0.0712	70	6.766	0.352	2.447	2.556	-23.5
(20) Massalia	1342224165	ChopNod	2455757.13413	2455757.13460	red	1.6812	0.0547	160	1.586	0.096	2.447	2.556	-23.5
(20) Massalia	1342224166	Scanmap	2455757.13679	2455757.13980	blue	6.8541	0.0687	70	6.820	0.354	2.447	2.556	-23.5
(20) Massalia	1342224166	Scanmap	2455757.13679	2455757.13980	red	1.7956	0.0222	160	1.694	0.089	2.447	2.556	-23.5
(20) Massalia	1342224167	Scanmap	2455757.14083	2455757.14384	blue	6.7438	0.0676	70	6.710	0.349	2.447	2.556	-23.5
(20) Massalia	1342224167	Scanmap	2455757.14083	2455757.14384	red	1.7820	0.0221	160	1.681	0.088	2.447	2.556	-23.5
(20) Massalia	1342224168	ChopNod	2455757.14481	2455757.14529	green	3.8860	0.0437	100	3.791	0.198	2.447	2.556	-23.5
(20) Massalia	1342224168	ChopNod	2455757.14481	2455757.14529	red	1.7582	0.0549	160	1.659	0.099	2.447	2.556	-23.5
(20) Massalia	1342224169	Scanmap	2455757.14747	2455757.15048	green	3.8115	0.0384	100	3.719	0.193	2.447	2.556	-23.5
(20) Massalia	1342224169	Scanmap	2455757.14747	2455757.15048	red	1.7494	0.0218	160	1.650	0.087	2.447	2.556	-23.5
(20) Massalia	1342224170	Scanmap	2455757.15151	2455757.15452	green	3.7704	0.0380	100	3.678	0.191	2.447	2.556	-23.5
(20) Massalia	1342224170	Scanmap	2455757.15151	2455757.15452	red	1.7234	0.0216	160	1.626	0.085	2.447	2.556	-23.5
(20) Massalia	1342241347	ChopNod	2456000.38816	2456000.38863	blue	5.6692	0.0605	70	5.641	0.294	2.721	2.866	20.5
(20) Massalia	1342241347	ChopNod	2456000.38816	2456000.38863	red	1.3470	0.0537	160	1.271	0.082	2.721	2.866	20.5
(20) Massalia	1342241348	Scanmap	2456000.39082	2456000.39382	blue	5.6602	0.0567	70	5.632	0.293	2.721	2.866	20.5
(20) Massalia	1342241348	Scanmap	2456000.39082	2456000.39382	red	1.4930	0.0198	160	1.409	0.074	2.721	2.866	20.5
(20) Massalia	1342241349	Scanmap	2456000.39486	2456000.39786	blue	5.6991	0.0571	70	5.671	0.295	2.721	2.866	20.5
(20) Massalia	1342241349	Scanmap	2456000.39486	2456000.39786	red	1.5196	0.0200	160	1.434	0.075	2.721	2.866	20.5
(20) Massalia	1342241350	ChopNod	2456000.39884	2456000.39931	green	3.3662	0.0392	100	3.284	0.172	2.721	2.866	20.5
(20) Massalia	1342241350	ChopNod	2456000.39884	2456000.39931	red	1.4226	0.0539	160	1.342	0.085	2.721	2.866	20.5
(20) Massalia	1342241351	Scanmap	2456000.40150	2456000.40451	green	3.3433	0.0338	100	3.262	0.170	2.721	2.866	20.5
(20) Massalia	1342241351	Scanmap	2456000.40150	2456000.40451	red	1.5477	0.0202	160	1.460	0.077	2.721	2.866	20.5
(20) Massalia	1342241352	Scanmap	2456000.40554	2456000.40855	green	3.3796	0.0342	100	3.297	0.171	2.721	2.866	20.5
(20) Massalia	1342241352	Scanmap	2456000.40554	2456000.40855	red	1.5510	0.0202	160	1.463	0.077	2.721	2.866	20.5
(20) Massalia	1342252017	ChopNod	2456202.54774	2456202.54821	green	4.3600	0.0480	100	4.254	0.222	2.726	2.510	-21.7
(20) Massalia	1342252017	ChopNod	2456202.54774	2456202.54821	red	1.9729	0.0556	160	1.861	0.108	2.726	2.510	-21.7
(20) Massalia	1342252018	Scanmap	2456202.55040	2456202.55341	green	4.3454	0.0437	100	4.239	0.220	2.726	2.510	-21.7
(20) Massalia	1342252018	Scanmap	2456202.55040	2456202.55341	red	1.9854	0.0237	160	1.873	0.098	2.726	2.510	-21.7
(20) Massalia	1342252019	Scanmap	2456202.55444	2456202.55745	green	4.2912	0.0432	100	4.186	0.218	2.726	2.510	-21.7
(20) Massalia	1342252019	Scanmap	2456202.55444	2456202.55745	red	1.9827	0.0237	160	1.871	0.098	2.726	2.510	-21.7
(20) Massalia	1342252020	ChopNod	2456202.55843	2456202.55890	blue	7.1802	0.0748	70	7.144	0.372	2.726	2.510	-21.7
(20) Massalia	1342252020	ChopNod	2456202.55843	2456202.55890	red	1.9093	0.0554	160	1.801	0.106	2.726	2.510	-21.7
(20) Massalia	1342252021	Scanmap	2456202.56108	2456202.56409	blue	7.4156	0.0743	70	7.379	0.383	2.726	2.510	-21.7
(20) Massalia	1342252021	Scanmap	2456202.56108	2456202.56409	red	1.9671	0.0236	160	1.856	0.097	2.726	2.510	-21.7
(20) Massalia	1342252022	Scanmap	2456202.56512	2456202.56813	blue	7.3486	0.0736	70	7.312	0.380	2.726	2.510	-21.7
(20) Massalia	1342252022	Scanmap	2456202.56512	2456202.56813	red	1.9292	0.0233	160	1.820	0.095	2.726	2.510	-21.7
(29) Amphitrite	1342205032	ChopNod	2455462.39006	2455462.39053	blue	19.1908	0.1931	70	19.095	1.015	2.637	2.315	-22.4
(29) Amphitrite	1342205032	ChopNod	2455462.39006	2455462.39053	red	4.9996	0.0721	160	4.717	0.310	2.637	2.315	-22.4
(29) Amphitrite	1342205033	Scanmap	2455462.39272	2455462.39572	blue	19.4078	0.1941	70	19.311	1.026	2.637	2.315	-22.4
(29) Amphitrite	1342205033	Scanmap	2455462.39272	2455462.39572	red	5.0909	0.0525	160	4.803	0.311	2.637	2.315	-22.4
(29) Amphitrite	1342205034	Scanmap	2455462.39675	2455462.39976	blue	19.2672	0.1927	70	19.171	0.996	2.637	2.315	-22.4
(29) Amphitrite	1342205034	Scanmap	2455462.39675	2455462.39976	red	5.0672	0.0523	160	4.780	0.249	2.637	2.315	-22.4
(29) Amphitrite	1342205035	ChopNod	2455462.40074	2455462.40121	green	10.9087	0.1109	100	10.643	0.553	2.637	2.315	-22.4
(29) Amphitrite	1342205035	ChopNod	2455462.40074	2455462.40121	red	4.8334	0.0710	160	4.560	0.242	2.637	2.315	-22.4
(29) Amphitrite	1342205036	Scanmap	2455462.40340	2455462.40641	green	10.9059	0.1092	100	10.640	0.553	2.637	2.315	-22.4
(29) Amphitrite	1342205036	Scanmap	2455462.40340	2455462.40641	red	4.9991	0.0517	160	4.716	0.245	2.637	2.315	-22.4
(29) Amphitrite	1342205037	Scanmap	2455462.40744	2455462.41045	green	10.8409	0.1085	100	10.576	0.550	2.637	2.315	-22.4
(29) Amphitrite	1342205037	Scanmap	2455462.40744	2455462.41045	red	5.0059	0.0517	160	4.723	0.246	2.637	2.315	-22.4
(52) Europa	1342191110	ChopNod	2455251.47051	2455251.47098	green	31.3568	0.3142	100	30.592	1.590	2.773	2.324	-20.2

Target	Obs. ID	Obs. mode	t_s (JD)	t_e (JD)	Band	$\langle f \rangle_\lambda$ (Jy)	$\sigma \langle f \rangle_\lambda$ (Jy)	λ (μm)	f_λ (Jy)	σf_λ (Jy)	r (au)	Δ (au)	α (deg.)
(52) Europa	1342191110	ChopNod	2455251.47051	2455251.47098	red	14.3521	0.1527	160	13.540	0.705	2.773	2.324	-20.2
(52) Europa	1342191111	Scanmap	2455251.47317	2455251.47606	green	31.8429	0.3185	100	31.066	1.614	2.773	2.324	-20.2
(52) Europa	1342191111	Scanmap	2455251.47317	2455251.47606	red	14.6886	0.1475	160	13.857	0.720	2.773	2.324	-20.2
(52) Europa	1342191112	Scanmap	2455251.47709	2455251.47998	green	31.7680	0.3177	100	30.993	1.611	2.773	2.324	-20.2
(52) Europa	1342191112	Scanmap	2455251.47709	2455251.47998	red	14.6980	0.1476	160	13.866	0.721	2.773	2.324	-20.2
(52) Europa	1342191113	ChopNod	2455251.48096	2455251.48143	blue	54.9117	0.5495	70	54.639	2.839	2.773	2.324	-20.2
(52) Europa	1342191113	ChopNod	2455251.48096	2455251.48143	red	14.4747	0.1538	160	13.655	0.711	2.773	2.324	-20.2
(52) Europa	1342191114	Scanmap	2455251.48362	2455251.48651	blue	55.1936	0.5520	70	54.919	2.854	2.773	2.325	-20.2
(52) Europa	1342191114	Scanmap	2455251.48362	2455251.48651	red	14.8255	0.1488	160	13.986	0.727	2.773	2.325	-20.2
(52) Europa	1342191115	Scanmap	2455251.48754	2455251.49043	blue	55.2985	0.5530	70	55.023	2.859	2.773	2.325	-20.2
(52) Europa	1342191115	Scanmap	2455251.48754	2455251.49043	red	14.7799	0.1484	160	13.943	0.725	2.773	2.325	-20.2
(52) Europa	1342212774	ChopNod	2455578.31503	2455578.31551	green	21.2908	0.2138	100	20.771	1.079	2.907	2.505	19.4
(52) Europa	1342212774	ChopNod	2455578.31503	2455578.31551	red	9.6031	0.1092	160	9.059	0.473	2.907	2.505	19.4
(52) Europa	1342212775	Scanmap	2455578.31769	2455578.32070	green	22.0940	0.2210	100	21.555	1.120	2.907	2.505	19.4
(52) Europa	1342212775	Scanmap	2455578.31769	2455578.32070	red	10.2926	0.1037	160	9.710	0.505	2.907	2.505	19.4
(52) Europa	1342212776	Scanmap	2455578.32173	2455578.32474	green	21.9317	0.2194	100	21.397	1.112	2.907	2.505	19.4
(52) Europa	1342212776	Scanmap	2455578.32173	2455578.32474	red	10.2345	0.1032	160	9.655	0.502	2.907	2.505	19.4
(52) Europa	1342212777	ChopNod	2455578.32572	2455578.32619	blue	36.6076	0.3667	70	36.425	1.893	2.907	2.505	19.4
(52) Europa	1342212777	ChopNod	2455578.32572	2455578.32619	red	10.0276	0.1130	160	9.460	0.494	2.907	2.505	19.4
(52) Europa	1342212778	Scanmap	2455578.32837	2455578.33138	blue	36.7495	0.3675	70	36.567	1.900	2.907	2.505	19.4
(52) Europa	1342212778	Scanmap	2455578.32837	2455578.33138	red	10.1105	0.1019	160	9.538	0.496	2.907	2.505	19.4
(52) Europa	1342212779	Scanmap	2455578.33241	2455578.33542	blue	36.8369	0.3684	70	36.654	1.905	2.907	2.505	19.4
(52) Europa	1342212779	Scanmap	2455578.33241	2455578.33542	red	10.0086	0.1009	160	9.442	0.491	2.907	2.505	19.4
(52) Europa	1342223194	Scanmap	2455736.71349	2455736.71650	blue	24.3770	0.2438	70	24.256	1.260	3.066	2.860	-19.6
(52) Europa	1342223194	Scanmap	2455736.71349	2455736.71650	red	6.6407	0.0677	160	6.265	0.326	3.066	2.860	-19.6
(52) Europa	1342223195	Scanmap	2455736.71753	2455736.72054	blue	24.1829	0.2419	70	24.063	1.250	3.066	2.860	-19.6
(52) Europa	1342223195	Scanmap	2455736.71753	2455736.72054	red	6.5975	0.0672	160	6.224	0.324	3.066	2.860	-19.6
(52) Europa	1342223196	Scanmap	2455736.72157	2455736.72458	green	14.2196	0.1423	100	13.873	0.721	3.066	2.860	-19.6
(52) Europa	1342223196	Scanmap	2455736.72157	2455736.72458	red	6.5915	0.0672	160	6.218	0.323	3.066	2.860	-19.6
(52) Europa	1342223197	Scanmap	2455736.72561	2455736.72862	green	14.2814	0.1429	100	13.933	0.724	3.066	2.860	-19.6
(52) Europa	1342223197	Scanmap	2455736.72561	2455736.72862	red	6.5634	0.0669	160	6.192	0.322	3.066	2.860	-19.6
(52) Europa	1342239463	ChopNod	2455972.44002	2455972.44049	green	12.3770	0.1254	100	12.075	0.628	3.292	3.574	16.0
(52) Europa	1342239463	ChopNod	2455972.44002	2455972.44049	red	5.6691	0.0769	160	5.348	0.282	3.292	3.574	16.0
(52) Europa	1342239464	Scanmap	2455972.44268	2455972.44569	green	12.1872	0.1220	100	11.890	0.618	3.292	3.574	16.0
(52) Europa	1342239464	Scanmap	2455972.44268	2455972.44569	red	5.7041	0.0585	160	5.381	0.280	3.292	3.574	16.0
(52) Europa	1342239465	Scanmap	2455972.44672	2455972.44973	green	12.1747	0.1218	100	11.878	0.617	3.292	3.574	16.0
(52) Europa	1342239465	Scanmap	2455972.44672	2455972.44973	red	5.7365	0.0588	160	5.412	0.281	3.292	3.574	16.0
(52) Europa	1342239466	ChopNod	2455972.45071	2455972.45118	blue	21.2326	0.2134	70	21.127	1.098	3.292	3.574	16.0
(52) Europa	1342239466	ChopNod	2455972.45071	2455972.45118	red	5.7149	0.0773	160	5.391	0.284	3.292	3.574	16.0
(52) Europa	1342239467	Scanmap	2455972.45336	2455972.45637	blue	20.8199	0.2082	70	20.716	1.077	3.292	3.574	16.0
(52) Europa	1342239467	Scanmap	2455972.45336	2455972.45637	red	5.7542	0.0590	160	5.428	0.282	3.292	3.574	16.0
(52) Europa	1342239468	Scanmap	2455972.45740	2455972.46041	blue	20.9489	0.2095	70	20.845	1.083	3.292	3.574	16.0
(52) Europa	1342239468	Scanmap	2455972.45740	2455972.46041	red	5.7686	0.0591	160	5.442	0.283	3.292	3.574	16.0
(52) Europa	1342250874	ChopNod	2456181.72811	2456181.72859	green	14.1364	0.1428	100	13.792	0.717	3.410	3.265	-17.3
(52) Europa	1342250874	ChopNod	2456181.72811	2456181.72859	red	6.3519	0.0821	160	5.992	0.315	3.410	3.265	-17.3
(52) Europa	1342250875	Scanmap	2456181.73077	2456181.73378	green	13.8624	0.1387	100	13.524	0.703	3.410	3.265	-17.3
(52) Europa	1342250875	Scanmap	2456181.73077	2456181.73378	red	6.4743	0.0660	160	6.108	0.318	3.410	3.265	-17.3
(52) Europa	1342250876	Scanmap	2456181.73481	2456181.73782	green	13.7449	0.1375	100	13.410	0.697	3.410	3.265	-17.3
(52) Europa	1342250876	Scanmap	2456181.73481	2456181.73782	red	6.4776	0.0661	160	6.111	0.318	3.410	3.265	-17.3

Table B.1. continued.

Target	Obs. ID	Obs. mode	t_s (JD)	t_e (JD)	Band	$\langle f \rangle_\lambda$ (Jy)	$\sigma \langle f \rangle_\lambda$ (Jy)	λ (μm)	f_λ (Jy)	σf_λ (Jy)	r (au)	Δ (au)	α (deg.)
(52) Europa	1342250877	ChopNod	2456181.73880	2456181.73927	blue	23.5759	0.2367	70	23.459	1.219	3.410	3.265	-17.3
(52) Europa	1342250877	ChopNod	2456181.73880	2456181.73927	red	6.3128	0.0818	160	5.955	0.313	3.410	3.265	-17.3
(52) Europa	1342250878	Scanmap	2456181.74145	2456181.74446	blue	23.1652	0.2317	70	23.050	1.198	3.410	3.265	-17.3
(52) Europa	1342250878	Scanmap	2456181.74145	2456181.74446	red	6.4660	0.0660	160	6.100	0.317	3.410	3.265	-17.3
(52) Europa	1342250879	Scanmap	2456181.74549	2456181.74850	blue	23.1100	0.2311	70	22.995	1.195	3.410	3.265	-17.3
(52) Europa	1342250879	Scanmap	2456181.74549	2456181.74850	red	6.4423	0.0657	160	6.078	0.316	3.410	3.265	-17.3
(52) Europa	1342270731	ChopNod	2456407.12182	2456407.12229	green	8.5334	0.0876	100	8.325	0.433	3.413	3.632	16.2
(52) Europa	1342270731	ChopNod	2456407.12182	2456407.12229	red	4.0052	0.0656	160	3.779	0.202	3.413	3.632	16.2
(52) Europa	1342270732	Scanmap	2456407.12447	2456407.12748	green	8.4388	0.0845	100	8.233	0.428	3.413	3.632	16.2
(52) Europa	1342270732	Scanmap	2456407.12447	2456407.12748	red	4.0020	0.0421	160	3.776	0.197	3.413	3.632	16.2
(52) Europa	1342270733	Scanmap	2456407.12851	2456407.13152	green	8.4216	0.0844	100	8.216	0.427	3.413	3.632	16.2
(52) Europa	1342270733	Scanmap	2456407.12851	2456407.13152	red	4.0240	0.0423	160	3.796	0.198	3.413	3.632	16.2
(52) Europa	1342270734	ChopNod	2456407.13250	2456407.13297	blue	14.3813	0.1453	70	14.310	0.744	3.413	3.632	16.2
(52) Europa	1342270734	ChopNod	2456407.13250	2456407.13297	red	3.6873	0.0637	160	3.479	0.187	3.413	3.632	16.2
(52) Europa	1342270735	Scanmap	2456407.13516	2456407.13816	blue	14.2226	0.1423	70	14.152	0.735	3.413	3.631	16.2
(52) Europa	1342270735	Scanmap	2456407.13516	2456407.13816	red	3.9915	0.0420	160	3.766	0.196	3.413	3.631	16.2
(52) Europa	1342270736	Scanmap	2456407.13920	2456407.14220	blue	14.1690	0.1417	70	14.098	0.733	3.413	3.631	16.2
(52) Europa	1342270736	Scanmap	2456407.13920	2456407.14220	red	4.0053	0.0421	160	3.779	0.197	3.413	3.631	16.2
(54) Alexandra	1342198509	Scanmap	2455365.31305	2455365.31606	blue	16.8546	0.1686	70	16.771	0.871	2.240	2.061	27.2
(54) Alexandra	1342198509	Scanmap	2455365.31305	2455365.31606	red	4.4740	0.0466	160	4.221	0.220	2.240	2.061	27.2
(54) Alexandra	1342198510	Scanmap	2455365.31709	2455365.32010	blue	16.8668	0.1687	70	16.783	0.872	2.240	2.061	27.2
(54) Alexandra	1342198510	Scanmap	2455365.31709	2455365.32010	red	4.4941	0.0468	160	4.240	0.221	2.240	2.061	27.2
(54) Alexandra	1342198511	Scanmap	2455365.32113	2455365.32414	green	9.7319	0.0974	100	9.495	0.493	2.240	2.061	27.2
(54) Alexandra	1342198511	Scanmap	2455365.32113	2455365.32414	red	4.4932	0.0468	160	4.239	0.221	2.240	2.061	27.2
(54) Alexandra	1342198512	Scanmap	2455365.32517	2455365.32818	green	9.7168	0.0973	100	9.480	0.493	2.240	2.061	27.2
(54) Alexandra	1342198512	Scanmap	2455365.32517	2455365.32818	red	4.4787	0.0466	160	4.225	0.220	2.240	2.061	27.2
(65) Cybele	1342188352	ChopNod	2455186.72070	2455186.72118	blue	12.8841	0.1305	70	12.820	0.666	3.471	3.575	-16.1
(65) Cybele	1342188352	ChopNod	2455186.72070	2455186.72118	red	3.4133	0.0622	160	3.220	0.174	3.471	3.575	-16.1
(65) Cybele	1342188353	ChopNod	2455186.72331	2455186.72378	green	7.5464	0.0781	100	7.362	0.383	3.471	3.575	-16.1
(65) Cybele	1342188353	ChopNod	2455186.72331	2455186.72378	red	3.3925	0.0621	160	3.200	0.173	3.471	3.575	-16.1
(65) Cybele	1342188354	Scanmap	2455186.72597	2455186.72860	blue	12.7986	0.1280	70	12.735	0.662	3.471	3.575	-16.1
(65) Cybele	1342188354	Scanmap	2455186.72597	2455186.72860	red	3.5283	0.0376	160	3.329	0.173	3.471	3.575	-16.1
(65) Cybele	1342188355	Scanmap	2455186.72964	2455186.73227	blue	12.7487	0.1275	70	12.685	0.659	3.471	3.575	-16.1
(65) Cybele	1342188355	Scanmap	2455186.72964	2455186.73227	red	3.5378	0.0377	160	3.337	0.174	3.471	3.575	-16.1
(65) Cybele	1342188356	Scanmap	2455186.73330	2455186.73594	green	7.5139	0.0753	100	7.331	0.381	3.471	3.575	-16.1
(65) Cybele	1342188356	Scanmap	2455186.73330	2455186.73594	red	3.5183	0.0375	160	3.319	0.173	3.471	3.575	-16.1
(65) Cybele	1342188357	Scanmap	2455186.73697	2455186.73961	green	7.5162	0.0753	100	7.333	0.381	3.471	3.575	-16.1
(65) Cybele	1342188357	Scanmap	2455186.73697	2455186.73961	red	3.5166	0.0375	160	3.317	0.173	3.471	3.575	-16.1
(65) Cybele	1342202949	Scanmap	2455421.39865	2455421.40166	blue	13.1617	0.1317	70	13.096	0.680	3.675	3.548	16.1
(65) Cybele	1342202949	Scanmap	2455421.39865	2455421.40166	red	3.7291	0.0395	160	3.518	0.183	3.675	3.548	16.1
(65) Cybele	1342202950	Scanmap	2455421.40269	2455421.40570	blue	13.1940	0.1320	70	13.128	0.682	3.675	3.548	16.1
(65) Cybele	1342202950	Scanmap	2455421.40269	2455421.40570	red	3.7174	0.0394	160	3.507	0.183	3.675	3.548	16.1
(65) Cybele	1342202951	Scanmap	2455421.40673	2455421.40974	green	7.8056	0.0782	100	7.615	0.396	3.675	3.548	16.1
(65) Cybele	1342202951	Scanmap	2455421.40673	2455421.40974	red	3.6949	0.0392	160	3.486	0.181	3.675	3.548	16.1
(65) Cybele	1342202952	Scanmap	2455421.41077	2455421.41378	green	7.8038	0.0782	100	7.614	0.396	3.675	3.548	16.1
(65) Cybele	1342202952	Scanmap	2455421.41077	2455421.41378	red	3.7048	0.0393	160	3.495	0.182	3.675	3.548	16.1
(65) Cybele	1342215367	ChopNod	2455627.36707	2455627.36754	blue	9.6119	0.0984	70	9.564	0.497	3.781	4.146	-13.5
(65) Cybele	1342215367	ChopNod	2455627.36707	2455627.36754	red	2.6562	0.0584	160	2.506	0.139	3.781	4.146	-13.5
(65) Cybele	1342215368	Scanmap	2455627.36973	2455627.37274	blue	9.4513	0.0946	70	9.404	0.489	3.781	4.146	-13.5

Target	Obs. ID	Obs. mode	t_s (JD)	t_e (JD)	Band	$\langle f \rangle_\lambda$ (Jy)	$\sigma \langle f \rangle_\lambda$ (Jy)	λ (μm)	f_λ (Jy)	σf_λ (Jy)	r (au)	Δ (au)	α (deg.)
(65) Cybele	1342215368	Scanmap	2455627.36973	2455627.37274	red	2.6832	0.0298	160	2.531	0.132	3.781	4.146	-13.5
(65) Cybele	1342215369	Scanmap	2455627.37377	2455627.37678	blue	9.4629	0.0947	70	9.416	0.489	3.781	4.146	-13.5
(65) Cybele	1342215369	Scanmap	2455627.37377	2455627.37678	red	2.6771	0.0298	160	2.526	0.132	3.781	4.146	-13.5
(65) Cybele	1342215370	ChopNod	2455627.37775	2455627.37823	green	5.6620	0.0600	100	5.524	0.288	3.781	4.146	-13.5
(65) Cybele	1342215370	ChopNod	2455627.37775	2455627.37823	red	2.6423	0.0583	160	2.493	0.139	3.781	4.146	-13.5
(65) Cybele	1342215371	Scanmap	2455627.38041	2455627.38342	green	5.6760	0.0570	100	5.538	0.288	3.781	4.146	-13.5
(65) Cybele	1342215371	Scanmap	2455627.38041	2455627.38342	red	2.7034	0.0300	160	2.550	0.133	3.781	4.146	-13.5
(65) Cybele	1342215372	Scanmap	2455627.38445	2455627.38746	green	5.6426	0.0566	100	5.505	0.286	3.781	4.146	-13.5
(65) Cybele	1342215372	Scanmap	2455627.38445	2455627.38746	red	2.6858	0.0298	160	2.534	0.132	3.781	4.146	-13.5
(88) Thisbe	1342203465	Scanmap	2455434.22809	2455434.23109	green	7.1442	0.0716	100	6.970	0.382	2.852	3.040	19.6
(88) Thisbe	1342203465	Scanmap	2455434.22809	2455434.23109	red	3.3680	0.0361	160	3.177	0.206	2.852	3.040	19.6
(88) Thisbe	1342203466	Scanmap	2455434.23212	2455434.23513	green	7.1493	0.0717	100	6.975	0.382	2.852	3.040	19.6
(88) Thisbe	1342203466	Scanmap	2455434.23212	2455434.23513	red	3.3840	0.0363	160	3.192	0.207	2.852	3.040	19.6
(88) Thisbe	1342203467	Scanmap	2455434.23616	2455434.23917	blue	12.2847	0.1229	70	12.224	0.635	2.852	3.040	19.6
(88) Thisbe	1342203467	Scanmap	2455434.23616	2455434.23917	red	3.4149	0.0365	160	3.222	0.168	2.852	3.040	19.6
(88) Thisbe	1342203468	Scanmap	2455434.24020	2455434.24321	blue	12.4207	0.1243	70	12.359	0.642	2.852	3.040	19.6
(88) Thisbe	1342203468	Scanmap	2455434.24020	2455434.24321	red	3.4361	0.0367	160	3.242	0.169	2.852	3.040	19.6
(88) Thisbe	1342234460	ChopNod	2455912.48111	2455912.48158	blue	12.6422	0.1282	70	12.579	0.654	3.213	2.827	17.5
(88) Thisbe	1342234460	ChopNod	2455912.48111	2455912.48158	red	3.4854	0.0626	160	3.288	0.178	3.213	2.827	17.5
(88) Thisbe	1342234461	Scanmap	2455912.48377	2455912.48678	blue	12.5462	0.1255	70	12.484	0.649	3.213	2.827	17.5
(88) Thisbe	1342234461	Scanmap	2455912.48377	2455912.48678	red	3.4906	0.0372	160	3.293	0.172	3.213	2.827	17.5
(88) Thisbe	1342234462	Scanmap	2455912.48781	2455912.49082	blue	12.4542	0.1246	70	12.392	0.644	3.213	2.827	17.5
(88) Thisbe	1342234462	Scanmap	2455912.48781	2455912.49082	red	3.4262	0.0366	160	3.232	0.168	3.213	2.827	17.5
(88) Thisbe	1342234463	ChopNod	2455912.49179	2455912.49227	green	7.3112	0.0758	100	7.133	0.371	3.213	2.827	17.5
(88) Thisbe	1342234463	ChopNod	2455912.49179	2455912.49227	red	3.1219	0.0607	160	2.945	0.161	3.213	2.827	17.5
(88) Thisbe	1342234464	Scanmap	2455912.49445	2455912.49746	green	7.1572	0.0717	100	6.983	0.363	3.213	2.827	17.5
(88) Thisbe	1342234464	Scanmap	2455912.49445	2455912.49746	red	3.3553	0.0360	160	3.165	0.165	3.213	2.827	17.5
(88) Thisbe	1342234465	Scanmap	2455912.49849	2455912.50150	green	7.0523	0.0707	100	6.880	0.357	3.213	2.827	17.5
(88) Thisbe	1342234465	Scanmap	2455912.49849	2455912.50150	red	3.2955	0.0354	160	3.109	0.162	3.213	2.827	17.5
(88) Thisbe	1342246229	ChopNod	2456075.76711	2456075.76758	green	5.7183	0.0606	100	5.579	0.290	3.103	3.057	-19.1
(88) Thisbe	1342246229	ChopNod	2456075.76711	2456075.76758	red	2.5403	0.0579	160	2.397	0.134	3.103	3.057	-19.1
(88) Thisbe	1342246230	Scanmap	2456075.76976	2456075.77277	green	5.7043	0.0573	100	5.565	0.289	3.103	3.057	-19.1
(88) Thisbe	1342246230	Scanmap	2456075.76976	2456075.77277	red	2.6905	0.0299	160	2.538	0.133	3.103	3.057	-19.1
(88) Thisbe	1342246231	Scanmap	2456075.77380	2456075.77681	green	5.7388	0.0576	100	5.599	0.291	3.103	3.057	-19.1
(88) Thisbe	1342246231	Scanmap	2456075.77380	2456075.77681	red	2.7151	0.0301	160	2.561	0.134	3.103	3.057	-19.1
(88) Thisbe	1342246232	ChopNod	2456075.77779	2456075.77826	blue	9.7729	0.1000	70	9.724	0.506	3.103	3.057	-19.1
(88) Thisbe	1342246232	ChopNod	2456075.77779	2456075.77826	red	2.4828	0.0576	160	2.342	0.131	3.103	3.057	-19.1
(88) Thisbe	1342246233	Scanmap	2456075.78045	2456075.78345	blue	9.6699	0.0968	70	9.622	0.500	3.103	3.057	-19.1
(88) Thisbe	1342246233	Scanmap	2456075.78045	2456075.78345	red	2.7083	0.0300	160	2.555	0.133	3.103	3.057	-19.1
(88) Thisbe	1342246234	Scanmap	2456075.78449	2456075.78749	blue	9.6333	0.0964	70	9.585	0.498	3.103	3.057	-19.1
(88) Thisbe	1342246234	Scanmap	2456075.78449	2456075.78749	red	2.6853	0.0298	160	2.533	0.132	3.103	3.057	-19.1
(88) Thisbe	1342261457	ChopNod	2456311.51224	2456311.51272	green	7.5224	0.0778	100	7.339	0.382	2.768	3.016	19.1
(88) Thisbe	1342261457	ChopNod	2456311.51224	2456311.51272	red	3.3025	0.0616	160	3.116	0.169	2.768	3.016	19.1
(88) Thisbe	1342261458	Scanmap	2456311.51490	2456311.51791	green	7.3777	0.0739	100	7.198	0.374	2.768	3.016	19.1
(88) Thisbe	1342261458	Scanmap	2456311.51490	2456311.51791	red	3.4350	0.0367	160	3.241	0.169	2.768	3.016	19.1
(88) Thisbe	1342261459	Scanmap	2456311.51894	2456311.52195	green	7.2630	0.0728	100	7.086	0.368	2.768	3.016	19.1
(88) Thisbe	1342261459	Scanmap	2456311.51894	2456311.52195	red	3.3855	0.0363	160	3.194	0.166	2.768	3.016	19.1
(88) Thisbe	1342261460	ChopNod	2456311.52293	2456311.52340	blue	12.4087	0.1259	70	12.347	0.642	2.768	3.016	19.1
(88) Thisbe	1342261460	ChopNod	2456311.52293	2456311.52340	red	3.0237	0.0602	160	2.853	0.156	2.768	3.016	19.1

Table B.1. continued.

Target	Obs. ID	Obs. mode	t_s (JD)	t_e (JD)	Band	$\langle f \rangle_\lambda$ (Jy)	$\sigma \langle f \rangle_\lambda$ (Jy)	λ (μm)	f_λ (Jy)	σf_λ (Jy)	r (au)	Δ (au)	α (deg.)
(88) Thisbe	1342261461	Scanmap	2456311.52559	2456311.52859	blue	12.1697	0.1218	70	12.109	0.629	2.768	3.016	19.1
(88) Thisbe	1342261461	Scanmap	2456311.52559	2456311.52859	red	3.3293	0.0357	160	3.141	0.164	2.768	3.016	19.1
(88) Thisbe	1342261462	Scanmap	2456311.52962	2456311.53263	blue	12.0804	0.1209	70	12.020	0.625	2.768	3.016	19.1
(88) Thisbe	1342261462	Scanmap	2456311.52962	2456311.53263	red	3.3148	0.0356	160	3.127	0.163	2.768	3.016	19.1
(93) Minerva	1342204236	Scanmap	2455449.34794	2455449.35094	green	2.6574	0.0270	100	2.593	0.135	3.121	3.366	17.5
(93) Minerva	1342204236	Scanmap	2455449.34794	2455449.35094	red	1.2459	0.0180	160	1.175	0.062	3.121	3.366	17.5
(93) Minerva	1342204237	Scanmap	2455449.35197	2455449.35498	green	2.6351	0.0268	100	2.571	0.134	3.121	3.365	17.5
(93) Minerva	1342204237	Scanmap	2455449.35197	2455449.35498	red	1.2237	0.0179	160	1.154	0.061	3.121	3.365	17.5
(93) Minerva	1342204238	Scanmap	2455449.35601	2455449.35902	blue	4.4997	0.0452	70	4.477	0.233	3.121	3.365	17.5
(93) Minerva	1342204238	Scanmap	2455449.35601	2455449.35902	red	1.2596	0.0181	160	1.188	0.063	3.121	3.365	17.5
(93) Minerva	1342204239	Scanmap	2455449.36005	2455449.36306	blue	4.5209	0.0454	70	4.498	0.234	3.121	3.365	17.5
(93) Minerva	1342204239	Scanmap	2455449.36005	2455449.36306	red	1.2479	0.0180	160	1.177	0.062	3.121	3.365	17.5
(423) Diotima	1342191019	ChopNod	2455250.91583	2455250.91630	blue	7.3959	0.0769	70	7.359	0.383	3.183	3.121	-18.2
(423) Diotima	1342191019	ChopNod	2455250.91583	2455250.91630	red	2.1154	0.0561	160	1.996	0.115	3.183	3.121	-18.2
(423) Diotima	1342191020	Scanmap	2455250.91849	2455250.92138	blue	7.5514	0.0756	70	7.514	0.391	3.183	3.121	-18.2
(423) Diotima	1342191020	Scanmap	2455250.91849	2455250.92138	red	2.1396	0.0250	160	2.018	0.106	3.183	3.121	-18.2
(423) Diotima	1342191021	Scanmap	2455250.92241	2455250.92531	blue	7.5443	0.0755	70	7.507	0.390	3.183	3.121	-18.2
(423) Diotima	1342191021	Scanmap	2455250.92241	2455250.92531	red	2.1385	0.0250	160	2.018	0.105	3.183	3.121	-18.2
(423) Diotima	1342191022	ChopNod	2455250.92628	2455250.92676	green	4.4976	0.0492	100	4.388	0.229	3.183	3.121	-18.2
(423) Diotima	1342191022	ChopNod	2455250.92628	2455250.92676	red	2.0593	0.0559	160	1.943	0.112	3.183	3.121	-18.2
(423) Diotima	1342191023	Scanmap	2455250.92894	2455250.93183	green	4.4689	0.0450	100	4.360	0.227	3.183	3.121	-18.2
(423) Diotima	1342191023	Scanmap	2455250.92894	2455250.93183	red	2.1231	0.0249	160	2.003	0.105	3.183	3.121	-18.2
(423) Diotima	1342191024	Scanmap	2455250.93287	2455250.93576	green	4.3672	0.0440	100	4.261	0.221	3.183	3.121	-18.2
(423) Diotima	1342191024	Scanmap	2455250.93287	2455250.93576	red	2.0830	0.0246	160	1.965	0.103	3.183	3.121	-18.2
(511) Davida	1342217773	Scanmap	2455652.00901	2455652.01202	blue	15.5278	0.1553	70	15.450	0.803	3.756	3.610	15.6
(511) Davida	1342217773	Scanmap	2455652.00901	2455652.01202	red	4.4116	0.0460	160	4.162	0.217	3.756	3.610	15.6
(511) Davida	1342217774	Scanmap	2455652.01305	2455652.01606	blue	15.4842	0.1549	70	15.407	0.801	3.756	3.610	15.6
(511) Davida	1342217774	Scanmap	2455652.01305	2455652.01606	red	4.3869	0.0458	160	4.139	0.215	3.756	3.610	15.6
(511) Davida	1342217775	Scanmap	2455652.01709	2455652.02010	green	9.2793	0.0929	100	9.053	0.470	3.756	3.610	15.6
(511) Davida	1342217775	Scanmap	2455652.01709	2455652.02010	red	4.3750	0.0456	160	4.127	0.215	3.756	3.610	15.6
(511) Davida	1342217776	Scanmap	2455652.02113	2455652.02414	green	9.2498	0.0926	100	9.024	0.469	3.756	3.610	15.6
(511) Davida	1342217776	Scanmap	2455652.02113	2455652.02414	red	4.3709	0.0456	160	4.123	0.215	3.756	3.610	15.6